Fast Transient Response of Series Resonant Converters Using Average Geometric Control

Mehdi Mohammadi, *Student Member, IEEE*, and Martin Ordonez, *Member, IEEE*

***Abstract*—Linear controllers and small-signal modeling techniques have been used for over 40 years to control power electronic converters around the equilibrium operating point. Outside the quiescent area, the shortcomings of linear controllers are well known and include uncertain large-signal transient behavior and sluggish dynamic/recovery response. In particular, resonant converters have inherent large-signal behavior, making the transient performance of small-signal linear controllers poor. This paper develops a geometric controller based on large-signal modeling to achieve enhanced dynamic response of the series resonant converter (SRC). The proposed modeling strategy provides detailed insight into the behavior of the SRC and creates an analytical framework to successfully perform geometric control. A new geometric control law is mathematically derived using average circular trajectories producing accurate and fast dynamics during startup, sudden load or reference changes. In order to validate the theoretical analysis, experimental and simulation results of an SRC are presented and compared to those of a linear and a nonlinear controller. The dynamic response is, on average, over 100 times faster than that of the designed linear controller, while overshoot is virtually eliminated.**

***Index Terms*—Average large-signal model, fast transient, geometric control, improved dynamic, natural switching surface, series resonant converter (SRC).**

I. Introduction

In recent years, resonant converters have gained popularity in many applications such as power factor corrector systems [1], bidirectional converters as the interface between the battery packs and renewable sources in hybrid automobiles and photovoltaic systems [2]–[4], microrobot drivers [5], LED drivers [6]–[9], and battery chargers [10], [11]. Unlike pulse width modulation (PWM) converters, resonant converters transfer power through a high-frequency resonant tank making the dynamic and steady state much more intricate than the PWM converter counterpart. Such increased complexity makes design and control of resonant converters more challenging. The traditional strategy to control power converters involves small-signal modeling by performing perturbation and linearization. Since this technique only considers the converter operation around the equilibrium operating point, it cannot provide sufficient information related to the large-signal behavior of the system, resulting in a poor response outside the designed operating point [12]. In spite of such difficulties, small-signal and frequency analysis have been popular tools in modeling, design, and implementation due to their simplicity [13]. Following with the small-signal analysis trend, simplified models of series and parallel resonant converters have been presented based on first harmonic approximation, including transfer functions for both frequency and duty cycle [14]. Another technique that has been used are sampled data models that are employed to reduce the transient and steady-state errors by dynamically controlling the switching frequency [15]. By performing perturbation methods [16], a small-signal model is suggested for the series resonant converter (SRC). Also, a small-signal discrete time model using the microsynthesis technique is introduced in [17]. However, while all these techniques can describe the small-signal behavior of the SRC successfully, they are not able to provide sufficient information about the actual large-signal dynamic nature of the system.

In addition to linear controllers, some interesting nonlinear control strategies for SRC have been proposed in the literature [18]–[22]. A nonlinear controller tracking the converter's trajectory in state plane is proposed in [18]–[20], which actually controls the energy level of the resonant tank. Therefore, by monitoring the instantaneous energy into the resonant tank, a control law is obtained based on calculating the radius of the converter's state trajectories. By using the piecewise affine concept [21], the SRC is modeled and a nonlinear controller is proposed where the dynamic of the resonant tank is investigated. Since the outer voltage loop has a relatively large constant time, the dynamic of the system may be slower and mostly affects the start-up response of the converter. A piecewise affine technique [22] was employed with a hybrid SRC controller (dual-loop structure) to make the dynamic response of the converter faster.

A number of advanced nonlinear controllers with outstanding dynamic performance have been presented in the literature for PWM-type converters [23]–[29], but the resonant converters have not. For example, the second-order boundary control law and raster surface have been introduced for buck converters [23]–[26] to provide an enhanced dynamic response, but not explored for SRC converters. As well, the natural switching surface has been employed for PWM topologies (buck, boost, inverters, etc.) featuring rapid transient recovery [27]–[29] but never studied in the SRC. Therefore, opportunities to employ such advanced geometric techniques to capture the actual large-signal nature of SRC and obtain extreme dynamic response remain open.

This paper develops a novel average geometric control (AGC) method based on large-signal modeling to achieve enhanced dynamic response of the SRC, particularly under the large signal variations and the start-up conditions. The proposed

Manuscript received August 11, 2015; revised October 31, 2015; accepted November 14, 2015. Date of publication December 1, 2015; date of current version March 25, 2016. This work was supported by the Natural Sciences and Engineering Research Council, Canada. Recommended for publication by Associate Editor R. Redl.

The authors are with the Department of Electrical and Computer Engineering, The University of British Columbia, Vancouver, BC V6T 1Z4 Canada (e-mail: mehdi.mohammadi.m@ieee.org; mordonez@ieee.org).

Color versions of one or more of the figures in this paper are available online at http://ieeexplore.ieee.org.

Digital Object Identifier 10.1109/TPEL.2015.2504489

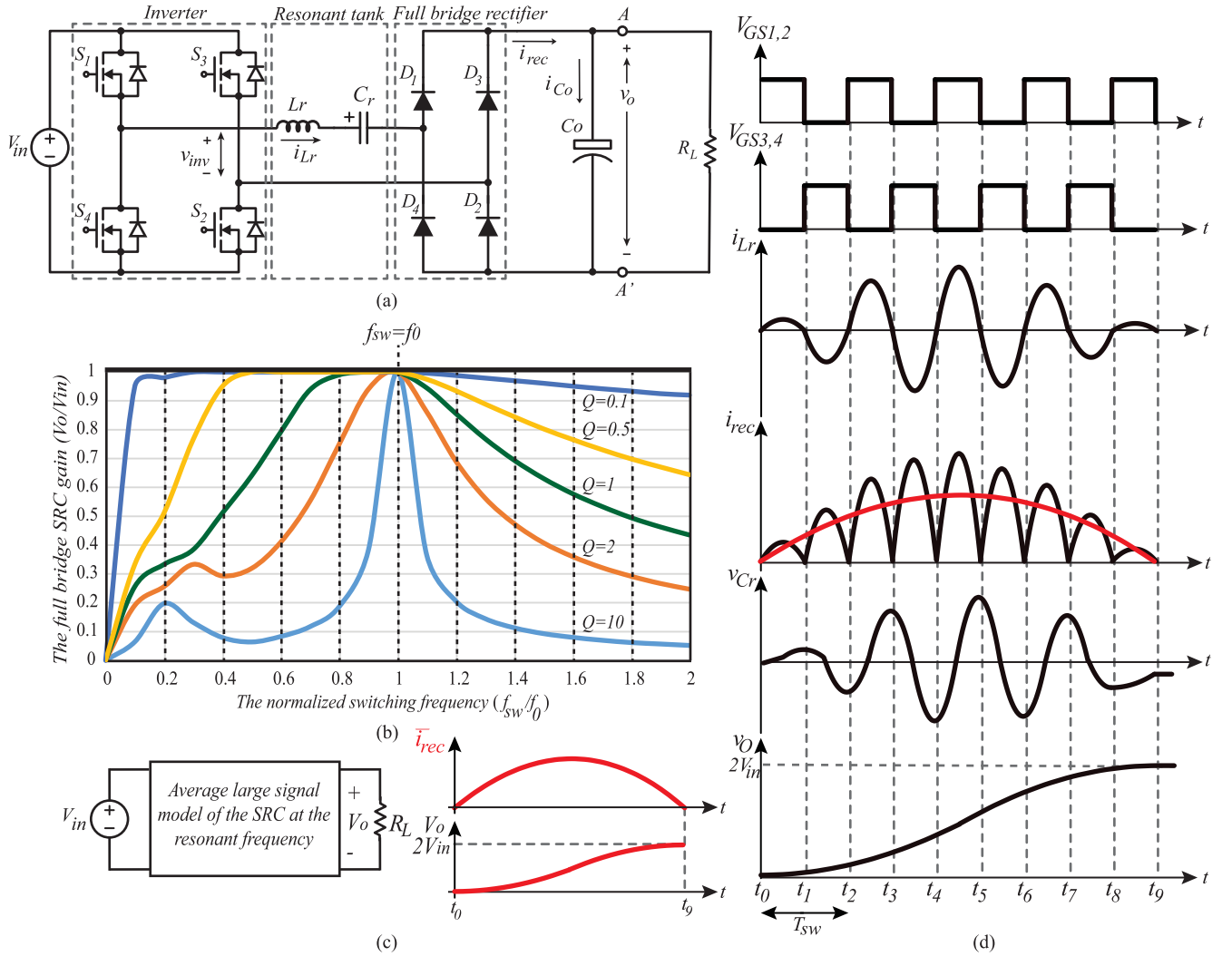

Fig. 1. (a) Full-bridge SRC. (b) SRC voltage gain versus the switching frequency under different load conditions. (c) Block diagram of the large-signal model of the SRC at the resonant frequency and its response in start-up and no-load condition. (d) SRC key waveforms in start-up and no-load condition at the resonant frequency.

AGC method has a low computational burden and simple current/voltage sensor requirements to achieve extreme transient performance. The large-signal geometric averaging significantly simplifies the analysis of the converter's dynamic behavior and brings the benefits of the geometric control surfaces to the SRC. The new geometric control law is mathematically derived using average circular trajectories producing accurate and fast dynamics during start-up, sudden load, or reference changes. The analytical AGC framework and theory are validated through experimental and simulation results and benchmarked against linear and rotating switching surfaces (RSS) controllers. On average, the dynamic response of the SRC using the proposed AGC method is over 100 times faster than that of the designed linear controller, while overshoot is virtually eliminated.

This paper is arranged into nine sections. In Section II, the average large-signal model of the SRC is derived. Using the derived model in Section II, the average circular trajectories are obtained in Section III. The normalized trajectories of the converter's model are engaged to investigate the dynamic response of the converter in startup and load, reference, and input voltage changes in Section IV. Also, in Section IV, the AGC law is introduced. In Section V, the AGC transient control strategy is discussed where a soft transition technique is used. The design procedure which provides a tool for the average large-signal model of the SRC to be used is presented in Section VI. In Section VII, the stability analysis is presented. To validate the theoretical analysis, the experimental and simulation results are presented in Section VIII. To put the issue into perspective, the conclusion is presented in Section IX.

II. Average Large-Signal Model

This section introduces the proposed SRC's large-signal model that will be employed to develop a controller with outstanding dynamic response and to obtain the average circular trajectories of the SRC. In order to elicit the proposed model, it is assumed that all of the converter's components in Fig. 1(a) are ideal. In Fig. 1(b), the full-bridge SRC gain versus the switching frequency for different load conditions is shown. According to the curves shown in Fig. 1(b), it is evident that the converter's gain not only depends on the switching frequency, but also varies significantly with the load effect on the quality factor

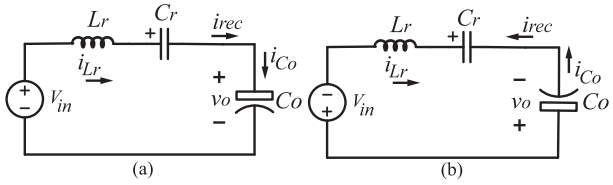

Fig. 2. Equivalent circuit of each SRC's structure at the resonant frequency. (a) Structure 1, (b) Structure 2.

$(Q = Z_0/R_L)$. In order to obtain the fastest response for the converter during transients including startup, load step-up and down, and also reference voltage step-up and down, the converter should work at the maximum and minimum gains while solving the transient. For the SRC, the maximum gain is met when the switching frequency equals the resonant frequency and the minimum gain is achieved when the inverter is in the OFF state. This mechanism will be used to model the large-signal behaving and obtain enhance transient performance.

As shown in Fig. 1(a), the full-bridge SRC has a resonant tank consisting an inductor and a capacitor (L_r and C_r). By considering the output filter capacitor, the number of the components storing energy is three. Hence, based on the configuration of these components, the order of the differential equations of the converter is three; however, under a specific condition, which will be described later in this section, the order of the system can be reduced to two since the converter has an average dynamic response. The key to see the system as a second-order system like the black box shown in Fig. 1(c) is to use the averaging technique.

The output of the SRC can be connected to any system, including a resistive load. However, according to the basic concepts of electrical circuit theory [30], to obtain the dynamic response of a linear circuit itself, a step input is applied to the circuit when all the initial conditions are zero. Because the large-signal behavior of the SRC is linear at the resonant frequency as shown in Section VIII-A, this concept can be used. Therefore, a step voltage (startup) in no-load condition can be applied to the SRC to calculate the dynamic response of the converter in the port AA' point of view.

To calculate the dynamic response of the SRC to the step input (startup), the converter's performance must be explained mathematically step by step. At the resonant frequency, the converter has two structures. Fig. 2 shows the equivalent circuits of each structure. As long as the converter works at the resonant frequency, the phase shift between the resonant current i_{Lr} and v_{inv} is zero. Conclusively, at the instant, the converter structure changes, the current through the resonant tank is zero. To obtain the converter's average large-signal model, it is considered that at the beginning of switching cycle 1, the converter is in zero initial conditions where $i_{Lr}(t_0)$, $v_{cr}(t_0)$, and $v_O(t_0)$ are all zero. The time t_k corresponds to the instant in which v_{inv} is inverted. k is a natural number and refers to the kth switching cycle. The time t_k is defined as follows:

$$t_k = k\pi\sqrt{L_r C_{\text{eq}}}, \quad k \in \{0, 1, 2, \ldots\} \tag{1}$$

where C_{eq} is the equivalent capacitor of C_r and C_O. C_{eq} will be calculated later. Note that the switching period T_{sw} equals $2\pi\sqrt{L_r C_{\text{eq}}}$.

By applying the input step (startup), the converter starts working and enters in the first switching cycle ($k = 0$). Since the structures of the converter repeat over each switching cycle, at the instant the structure 2 [see Fig. 2(b)] is switched to structure 1 [see Fig. 2(a)], k is increased by 1. Therefore, the converter's behavior can be explained in each half switching cycle as follows.

Half cycle $(k+1)$th $(t_k < t < t_{k+1})$: At t_k, the switches S_1 and S_2 and diodes D_1 and D_2 turn ON under zero current switching (ZCS) condition. Therefore, the voltage of v_{inv} becomes $+V_{\text{in}}$ and a voltage of $V_{\text{in}} - v_O(t_k)$ drops across the resonant tank. Consequently, the current through the resonant inductor increases in a sinusoidal manner with the direction shown in Fig. 2(a). The important equations of this half cycle are as follows:

$$i_{Lr}(t) = i_{\text{rec}}(t) = \frac{V_{\text{in}} - v_{Cr}(t_k) - v_O(t_k)}{Z_0}\sin[\omega_0(t - t_k)] \tag{2}$$

$$v_{Cr}(t) = \frac{C_{\text{eq}}}{C_r}[V_{\text{in}} - v_{Cr}(t_k) - v_O(t_k)][1 - \cos[\omega_0(t - t_k)]] \tag{3}$$

$$v_O(t) = \frac{C_{\text{eq}}}{C_r}[V_{\text{in}} - v_{Cr}(t_k) - v_O(t_k)][1 - \cos[\omega_0(t - t_k)]] + v_O(t_k) \tag{4}$$

where

$$\omega_0 = \frac{1}{\sqrt{L_r C_{\text{eq}}}} \tag{5}$$

$$Z_0 = \sqrt{\frac{L_r}{C_{\text{eq}}}} \tag{6}$$

$$C_{\text{eq}} = \frac{C_r C_O}{C_r + C_O}. \tag{7}$$

Half cycle $(k+2)$th $(t_{k+1} < t < t_{k+2})$: At t_{k+1}, the switches S_1 and S_2 are turned OFF and switches S_3 and S_4 are turned ON all under ZCS condition. Also, at the beginning of this mode, the diodes D_1 and D_2 turn OFF and diodes D_3 and D_4 turn ON under ZCS condition. Therefore, v_{inv} becomes $-V_{\text{in}}$ and a voltage of $-V_{\text{in}} + v_O(t_{k+1})$ drops across the resonant tank. Hence, $i_{Lr}(t)$ starts to increase in a sinusoidal manner with the opposite direction shown in Fig. 2(b). The important equations of this half cycle are as follows:

$$i_{Lr}(t) = -i_{\text{rec}}(t) = \frac{-V_{\text{in}} - v_{Cr}(t_{k+1}) + v_O(t_{k+1})}{Z_0}\sin[\omega_0(t - t_{k+1})] \tag{8}$$

$$v_{Cr}(t) = \frac{C_{\text{eq}}}{C_r}[-V_{\text{in}} - v_{Cr}(t_{k+1}) + v_O(t_{k+1})][1 - \cos[\omega_0(t - t_{k+1})]] + v_{Cr}(t_{k+1}) \tag{9}$$

$$v_{Co}(t) = \frac{C_{\text{eq}}}{C_O}[V_{\text{in}} + v_{Cr}(t_{k+1}) - v_O(t_{k+1})][1 - \cos[\omega_0(t - t_{k+1})] + v_O(t_{k+1}). \tag{10}$$

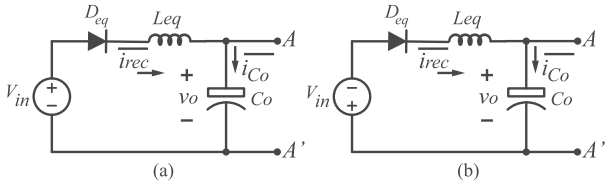

Fig. 3. Average large-signal model of the full-bridge SRC when (a) converter works at the resonant frequency and (b) when all of the converter switches are in OFF state.

According to the equations obtained above, the output and resonant capacitors' voltages at the end of each half cycle can be calculated by use of (11) and (12). Also, the current through the resonant inductor at the middle of each half cycle can be computed by (13)

$$v_O(t_k) = \sum_{n=1}^{k} \left[2\frac{C_{\rm eq}}{C_O} \left[V_{\rm in} + (-1)^n v_{Cr}(t_{n-1}) - v_O(t_{n-1}) \right] + v_O(t_{n-1}) \right] \tag{11}$$

$$v_{Cr}(t_k) = \sum_{n=1}^{k} \left[\frac{C_{\rm eq}}{C_r} \left[(-1)^{n+1} V_{\rm in} - v_{Cr}(t_{n-1}) + (-1)^n v_O(t_{n-1}) \right] + v_O(t_{n-1}) \right] \tag{12}$$

$$i_{Lr}\left(\frac{t_{2k-1}}{2}\right) = \frac{1}{Z_0} \sum_{n=1}^{k} \left[(-1)^{n+1} V_{\rm in} - v_{Cr}(t_{n-1}) + (-1)^n v_O(t_{n-1}) \right]. \tag{13}$$

Based on the obtained equations, particularly (11)–(13) that describe the dynamic response of the SRC to the step input, the theoretical waveforms of the converter in transient under no-load condition can be drawn as shown in Fig. 1(d). To draw the theoretical waveforms of the converter, it is assumed that $C_{\rm eq}/C_O = 1/30$. Although it will be calculated later in this section, the number of the current pulses (half cycles) required for the output voltage to reach to the twice of the input voltage is nine for this case.

Careful scrutiny in the output rectified current $i_{\rm rec}$ waveform reveals that the current follows a semicycle pattern which resembles the behavior of a second-order rectified LC circuit. Consequently, as the start point, it can be assumed that the circuits shown in Fig. 3(a) and (b) model the large-signal behavior of the converter when the inverter is in the ON and OFF states, respectively. This will be proven theoretically in following. In Fig. 3, all the components are known except $L_{\rm eq}$. Therefore, the problem here is to find the value of the equivalent inductor $L_{\rm eq}$.

If the circuit shown in Fig. 3(a) is a model of the SRC when its inverter is in the ON state and also works at the resonant frequency, a bridge should exist between these two circuits which results in finding the value of $L_{\rm eq}$. For this reason, the averaging technique can be performed on $i_{\rm rec}$ as follows, where the integral interval is $[t_0 - t_1]$:

$$\overline{i_{\rm rec(half)}} = \frac{2}{T_{\rm sw}} \int_{t_0}^{t_1} \frac{V_{\rm in}}{Z_0} \sin[\omega_0 (t - t_0)] dt. \tag{14}$$

Solving (14) results in the following:

$$\overline{i_{\rm rec(half)}} = \frac{4 V_{\rm in} C_{\rm eq}}{T_{\rm sw}}. \tag{15}$$

For the proposed model in Fig. 3(a), the current through $L_{\rm eq}$ with considering the zero initial conditions can be computed as follows:

$$\overline{i_{\rm rec}}(t) = \frac{V_{\rm in}}{Z_{\rm eq}} \sin[\omega_{\rm eq}(t - t_0)] \tag{16}$$

where

$$\omega_{\rm eq} = \frac{1}{\sqrt{L_{\rm eq} C_O}} \tag{17}$$

$$Z_{\rm eq} = \sqrt{\frac{L_{\rm eq}}{C_O}}. \tag{18}$$

Now, by performing the averaging technique with the interval of $[t_0 - t_1]$ on (16), we obtain

$$\overline{i_{\rm rec(half)}} = \frac{2}{T_{\rm sw}} \int_{t_0}^{t_1} \frac{V_{\rm in}}{Z_{\rm eq}} \sin[\omega_{\rm eq}(t - t_0)] dt. \tag{19}$$

Solving the equation above results in

$$\overline{i_{\rm rec(half)}} = \frac{2 V_{\rm in} C_O}{T_{\rm sw}} \left[1 - \cos(\pi \sqrt{\frac{L_r C_{\rm eq}}{L_{\rm eq} C_O}}) \right]. \tag{20}$$

Thus, for finding the value of $L_{\rm eq}$, (15) and (20) should be equal together. By combining (15) and (20), $L_{\rm eq}$ can be computed by use of the equation below

$$L_{\rm eq} = \frac{C_{\rm eq}}{C_O} \frac{\pi^2 L_r}{\left[\frac{\pi}{180} \cos^{-1}\left(1 - 2\frac{C_{\rm eq}}{C_O} \right) \right]^2}. \tag{21}$$

Drawing the current through $L_{\rm eq}$ results in the red waveform shown in Fig. 1(d). It will be discussed later that how $i_{\rm rec}$ can be sensed to be match with $\overline{i_{\rm rec}}$ waveform.

By use of (22), the number of the required current pulses n for the output voltage to reach to $2V_{\rm in}$ in start up can be calculated as follows:

$$n = \frac{180}{\cos^{-1}\left(1 - 2\frac{C_{\rm eq}}{C_O} \right)}. \tag{22}$$

As long as the inverter is in the ON state, the converter's model illustrated in Fig. 3(a) is valid. Upon turning OFF all the converter's switches, the model changes to the circuit shown in Fig. 3(b) due to the action of the switches' body diodes.

III. Normalized Average Circular Trajectories

Previously, the average large-signal model at the port AA' point of view was obtained. In this section, using the introduced model, the SRC's large-signal dynamic behavior is analyzed which will result in obtaining the average circular trajectories of the converter. The advantage of using the average circular trajectories is that the movement of the converter's operating point in state plane can be calculated and predicted and also it provides a powerful tool for analyzing the converter's performance in transients. Since the converter's dynamic behavior

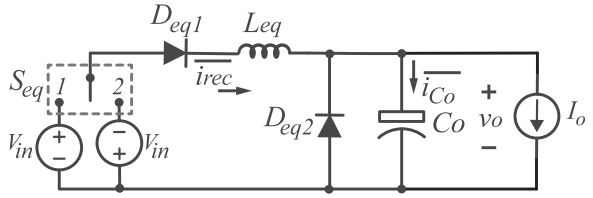

Fig. 4. Average large-signal model of the full-bridge SRC with a constant current load.

under a constant current load is similar to the case that the resistance of the load R_L equals infinity and in terms of stability, it resembles the worst case, a constant current load is applied to the model for providing a framework for the analysis. The two circuits shown in Fig. 3(a) and (b) can be combined together to obtain the average large-signal model of the converter as shown in Fig. 4. Working with the model shown in Fig. 4 makes the operation of the converter's model more understandable. In this circuit, the function of the power MOSFETs and their antiparallel diodes are modeled with S_{eq}. When S_{eq} is in the position 1, the inverter is in the ON state and when it is in the position 2, the inverter is in the OFF state. For more simplicity, hereafter, when it is stated that S_{eq} is in the ON or OFF states, it means that S_{eq} is in the position 1 or 2, respectively. The rectifier of the full-bridge SRC is modeled with D_{eq1} and D_{eq2}. In the circuit in Fig. 1(a), because the full-bridge rectifier is installed in parallel with the output capacitor C_O, the output voltage never becomes negative. That is why in the circuit in Fig. 4, D_{eq2} is installed in parallel with C_O. However, the constant current load I_O is selected for the converter analysis, it will be shown that the fast transient with no overshoot is not only achieved for the selected load but for any other resistive loads as well.

The general differential equation of the converter depicted in Fig. 4, which describes the converter's large-signal dynamic behavior, is given by the following equation:

$$\frac{d^2\overline{i_{\rm rec}}(t)}{dt^2}+\omega_{\rm eq}^2\overline{i_{\rm rec}}(t)=\omega_{\rm eq}^2 I_O. \tag{23}$$

$\overline{i_{\rm rec}}(t)$ in the time domain can be obtained from (24) where the initial conditions are $v_O(0)$ and $\overline{i_{\rm rec}}(0)$

$$\begin{aligned}\overline{i_{\rm rec}}(t)=&\ \frac{u(t)V_{\rm in}-v_O(0)}{Z_{\rm eq}}\sin(\omega_{\rm eq}t)\\&+\left[\overline{i_{\rm rec}}(0)-I_O\right]\cos(\omega_{\rm eq}t)+I_O\end{aligned} \tag{24}$$

where $u(t)$ is a function determining the state of S_{eq} and defined as follows:

$$u(t)=\begin{cases}1, & \text{if } S_{\rm eq}=\text{ON}\\ -1, & \text{if } S_{\rm eq}=\text{OFF}.\end{cases} \tag{25}$$

In order to simplify the analysis, all the voltages and currents and also the time t are normalized with the factors below

$$v_{xn}=\frac{v_x}{V_{\rm in}} \tag{26}$$

$$i_{xn}=\frac{i_x}{V_{\rm in}}Z_{\rm eq} \tag{27}$$

$$t_n=2\pi\frac{t}{T_{\rm eq}} \tag{28}$$

where $T_{\rm eq}=2\pi\sqrt{L_{\rm eq}C_O}$.

After performing the normalization, (24) can be rewritten as follows:

$$\begin{aligned}\overline{i_{\rm recn}}(t_n)=&\ [u(t_n)-v_{On}(t_{n0})]\sin(t_n)\\&+\left[\overline{i_{\rm recn}}(0)-I_{On}\right]\cos(t_n)+I_O n.\end{aligned} \tag{29}$$

Because $\overline{i_{C\rm on}}(t_n)=\overline{i_{\rm recn}}(t_n)-I_{On}$, (29) can be rearranged as follows:

$$\overline{i_{C\rm on}}(t_n)=[u(t_n)-v_{\rm on}(0)]\sin(t_n)+\overline{i_{C\rm on}}(0)\cos(t_n). \tag{30}$$

By using (30), the normalized output voltage v_{On} is derived as follows:

$$\begin{aligned}v_{On}(t_n)=&\ [u(t_n)-v_{On}(0)][1-\cos(t_n)]\\&+i_{C\rm on}(0)\sin(t_n)+v_{On}(0).\end{aligned} \tag{31}$$

Now, (31) can be rearranged as follows:

$$\begin{aligned}v_{On}(t_n)-u(t_n)=&\ -[u(t_n)-v_{On}(0)]\cos(t_n)\\&+i_{C\rm on}(0)\sin(t_n).\end{aligned} \tag{32}$$

If the terms γ and β are defined as follows:

$$\gamma=\ -[u(t_n)-v_{On}(0)] \tag{33}$$

$$\beta=\ i_{C\rm on}(0) \tag{34}$$

(32) results in the following equation:

$$v_{On}(t_n)-u(t_n)=\sqrt{\gamma^2+\beta^2}\sin\left[t_n+\tan^{-1}\left(\frac{\gamma}{\beta}\right)\right]. \tag{35}$$

From (35), $t_n+\tan^{-1}(\gamma/\beta)$ can be computed by the equation below:

$$t_n+\tan^{-1}(\gamma/\beta)=\sin^{-1}\left[\frac{v_{On}(t_n)-u(t_n)}{\sqrt{\gamma^2+\beta^2}}\right]. \tag{36}$$

By differentiating (35), the normalized output capacitor current is obtained as follows:

$$\begin{aligned}\frac{dv_{On}(t_n)}{dt_n}=\overline{i_{C\rm on}}(t_n)=&\sqrt{\overline{i_{C\rm on}}(0)^2+[v_{On}(0)-u(t_n)]^2}\\&\times\cos\left[\sin^{-1}\left(\frac{v_{On}(t_n)-u(t_n)}{\sqrt{\gamma^2+\beta^2}}\right)\right].\end{aligned} \tag{37}$$

Now, combining (36) and (37) results in the following equation:

$$\begin{aligned}\overline{i_{C\rm on}}(t_n)=&\ \sqrt{\overline{i_{C\rm on}}(0)^2+[v_{On}(0)-u(t_n)]^2}\\&\times\cos\left[\sin^{-1}\left(\frac{v_{\rm on}(t_n)-u(t_n)}{\sqrt{\gamma^2+\beta^2}}\right)\right].\end{aligned} \tag{38}$$

Since $\cos[\sin^{-1}(x)]=\sqrt{1-x^2}$, (38) can be written as follows, which actually describes the average trajectories of the converter:

$$\begin{aligned}\overline{i_{C\rm on}}^2(t_n)\ &+[v_{On}(t_n)-u(t_n)]^2=\overline{i_{C\rm on}}^2(0)\\&+[v_O n(0)-u(t_n)]^2.\end{aligned} \tag{39}$$

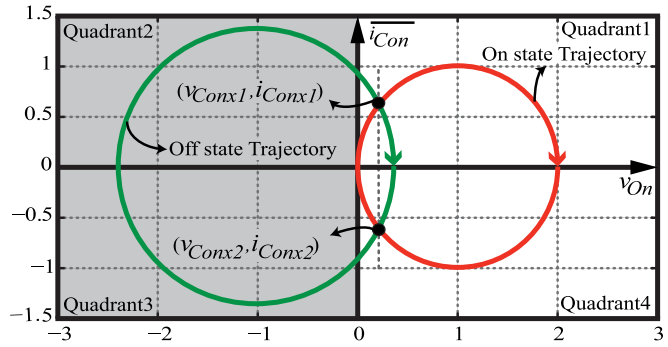

Fig. 5. ON and OFF state trajectories under two specific initial conditions.

Equation (39) represents an infinite number of circles with the radius of

$$\sqrt{\overline{i_{C\mathrm{on}}}^2(0) + [v_{On}(0) - u(t_n)]^2},$$

which is determined by the initial conditions and the state of S_{eq}. Also, the origin of the circles is $(v_{On}(t_n) - u(t_n), 0)$. Because (39) represents two sets of trajectories (ON and OFF state trajectories), the relationship between these two sets of trajectories should be identified. If the distance between the ON and OFF state circles is named O_1O_2, according to (39), $O_1O_2 = 2$. By naming the radius of the ON and OFF state trajectories r_1 and r_2 which equal

$$\sqrt{\overline{i_{C\mathrm{on}}}^2(0) + [v_{On}(0) - 1]^2}$$

and

$$\sqrt{\overline{i_{C\mathrm{on}}}^2(0) + [v_{On}(0) + 1]^2},$$

respectively, for $v_{On}(0) < 1$, (40) can be satisfied. The result of satisfying (40) is that it shows the ON and OFF state trajectories are two intersecting circles as shown in Fig. 5. Because of the existence of D_{eq2}, the output voltage cannot be negative. Therefore, the left side of the state plane depicted in Fig. 5 is highlighted to show that the converter cannot work in that region. Also, the direction of the circles' rotations is determined in Fig. 5

$$|r_1 - r_2| < O_1O_2 < r_1 + r_2. \tag{40}$$

IV. Transient Analysis and AGC Law

Referring to the obtained trajectories of the converter's model, in this section, the large-signal dynamic response of the converter's model in transient is discussed and, finally, a control law will be introduced. For this purpose, five scenarios are considered: the performance of the converter's model in start-up, load step-up and step-down, and also sudden reference voltage changes. In startup, the converter is in zero initial conditions which means that $v_{\mathrm{on}}(0)$ and $\overline{i_{C\mathrm{on}}}(0)$ are zero. Fig. 6 is utilized to explain the behavior of the converter's model in start up in both the state plane and time domain. By assuming that at turn-on instant, the converter is in no-load condition, at the point P_{a1}, S_{eq} turns ON and causes the converter to follow the ON state trajectory as shown in Fig. 6. Because the final destination for the

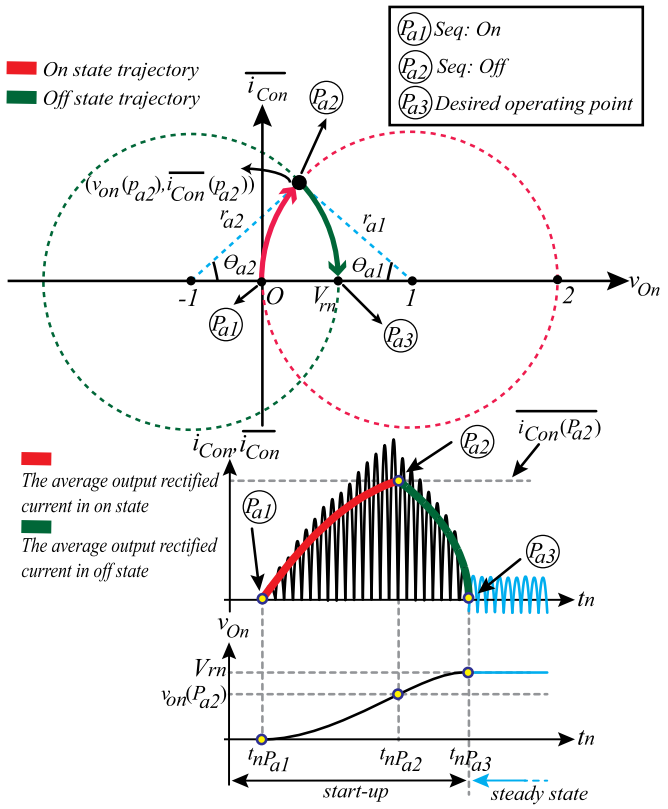

Fig. 6. Converter's start-up response in state plane and time domain.

converter is to reach to the desired operating point in which the output voltage equals the reference voltage and the average of the output capacitor current is zero, the OFF state trajectory that intersects the ON state trajectory and leads the converter to reach to this goal should be determined. Therefore, by knowing the desired OFF state trajectory, the intersection of the both trajectories can be obtained. At the point P_{a2} (the intersection point between the two trajectories), S_{eq} turns OFF; however, D_{eq1} remains ON. Then, the converter follows the OFF state trajectory as shown in Fig. 6. Finally, at the point P_{a3}, the output voltage and output capacitor current reach to the reference voltage and zero, respectively, without producing overshoot. At the point P_{a2}, the output voltage can be calculated by use of the equation below

$$v_{On}(P_{a2}) = \frac{1}{4} V_{rn}(V_{rn} + 2) \tag{41}$$

where V_{rn} is the normalized reference voltage. Because the circles shown in Fig. 6 rotates with the speed of the angular frequency, calculating θ_{a1} and θ_{a2} provides a preliminary to find the duration of startup. θ_{a1} and θ_{a2} can be calculated by the following equations:

$$\theta_{a1} = \cos^{-1}[1 - v_{On}(P_{a2})] \tag{42}$$

$$\theta_{a2} = \cos^{-1}\left[\frac{1 + v_{On}(P_{a2})}{1 + V_{rn}}\right]. \tag{43}$$

Although usually applying constant current load in start up does not happen in practice, its effect on the settling time can be assessed theoretically. Referring to Fig. 4, the diode D_{eq2} does

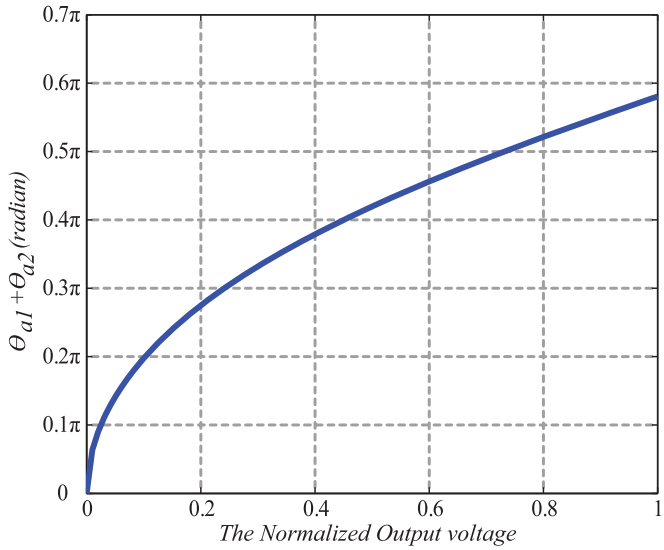

Fig. 7. $\theta_{a1}+\theta_{a2}$ versus the normalized reference voltage.

not allow the output voltage to be negative. Hence, due to the existence of $L_{\rm eq}$, applying a constant current load in start up causes D_{eq2} to turn-on. As long as the amplitude of the current through $L_{\rm eq}$ is not equal the constant current load I_O, the output voltage remains zero. Therefore, in this situation where $S_{\rm eq}$ is in the ON state, a positive voltage of $V_{\rm in}$ drops over $L_{\rm eq}$ causing its current to increase linearly. The instant in which the current through $L_{\rm eq}$ equals I_O can be calculated by use of the following equation:

$$t_{nPa1} = L_{\rm eq} I_{On}. \tag{44}$$

By taking into account the delay time t_{nPa1}, the time the output voltage takes to reach to the desired operating point can be calculated by use of the equation below. As (42) and (43) describe, θ_{a1} and θ_{a2} do not depend on the output current and just depend on the normalized reference voltage. In Fig. 7, $\theta_{a1}+\theta_{a2}$ versus the normalized reference voltage is plotted

$$t_{nPa3} = \frac{T_{\rm eq}}{2\pi}(\theta_{a1}+\theta_{a2}+t_{nPa1}). \tag{45}$$

Another scenario which is very important to analyze the converter's transient is sudden load step-up when the converter works in the desired operating point. To discuss on this term, Fig. 8 can be considered. By abruptly changing the load, the current through the output capacitor becomes negative and the operating point drops from $(V_{rn},0)$ to $(V_{rn},-\Delta I_{Lnb})$. Therefore, $S_{\rm eq}$ turns ON at the point P_{b1} and causes the converter pursues the ON state trajectory as shown in Fig. 8. At the point P_{b2} where is the intersection between the ON and OFF state trajectories, $S_{\rm eq}$ turns OFF and the OFF state trajectory is followed until the converter reaches to the desired operating point which is actually the point P_{b3}. Depending on the load added to the output, the interval the converter needs to reach again to the desired operating point can be calculated. For this reason, the angles θ_{b1}, θ_{b2},

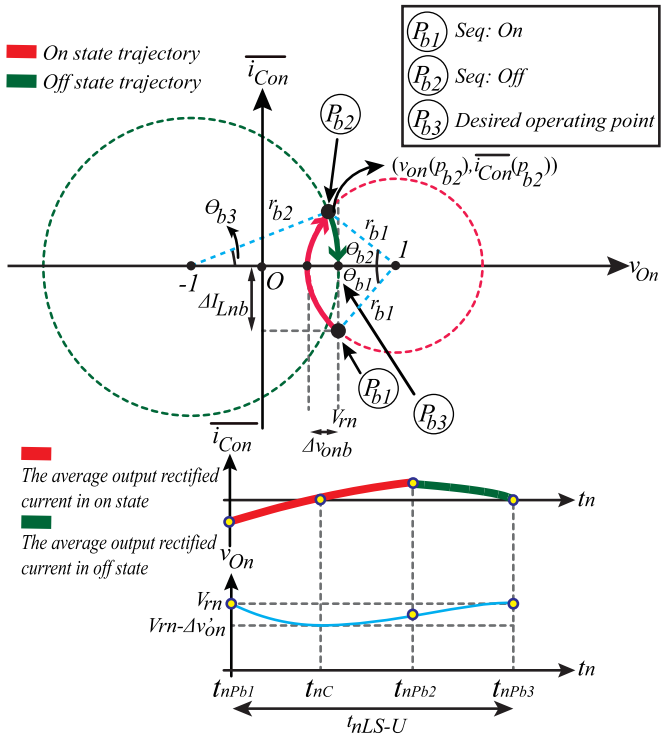

Fig. 8. Converter's transient response to load step-up in state plane and time domain.

and θ_{b3} can be computed by the following equations:

$$\theta_{b1} = \cos^{-1}\left(\frac{1-V_{rn}}{\sqrt{\Delta I_{Lnb}^2+(1-V_{rn})^2}}\right) \tag{46}$$

$$\theta_{b2} = \cos^{-1}\left(\frac{1-V_{rn}+(1/4)\Delta I_{Lnb}^2}{\sqrt{\Delta I_{Lnb}^2+(1-V_{rn})^2}}\right) \tag{47}$$

$$\theta_{b3} = \cos^{-1}\left(\frac{1+V_{rn}-(1/4)\Delta I_{Lnb}^2}{1+V_{rn}}\right). \tag{48}$$

Now that the angles θ_{b1}, θ_{b2}, and θ_{b3} have been obtained, the required time for the converter to reach to the desired point after load step-up can be calculated using the equation below:

$$t_{LS-U} = \frac{T_{\rm eq}}{2\pi}(\theta_{b1}+\theta_{b2}+\theta_{b3}). \tag{49}$$

Also, the normalized output voltage variation after load step-up is given in the following:

$$\Delta v_{\rm onb} = (1-V_{rn}) - \sqrt{\Delta I_{Lnb}^2+(1-V_{rn})^2}. \tag{50}$$

In Fig. 9, the variation of the normalized output voltage versus the load added to the output for different reference voltages is plotted.

The next scenario is analyzing the model's behavior in load step-down. To analyze the dynamic of the converter's model, Fig. 10 is utilized which illustrates the dynamic response of the converter's model in both state plane and time domain after applying load step-down. After load step-down, the operating point from $(V_{rn},0)$ jumps to $(V_{rn},\Delta I_{Lnc})$. In this case, $S_{\rm eq}$ turns OFF and the converter pursues the OFF state trajectory as

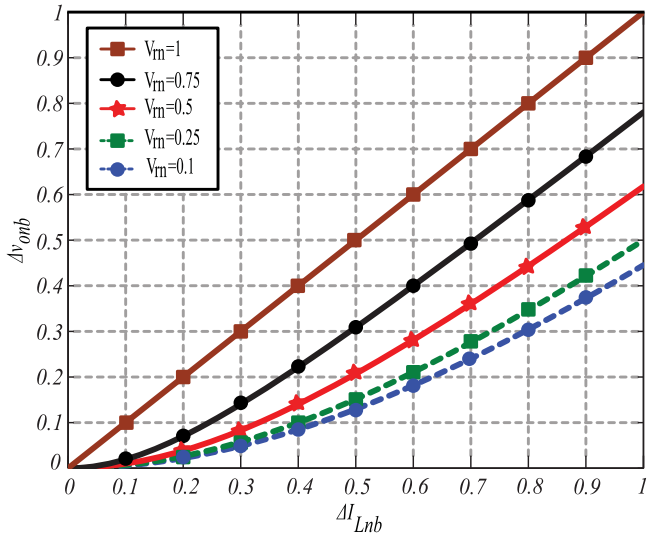

Fig. 9. Normalized output voltage's variation versus the load added to the converter.

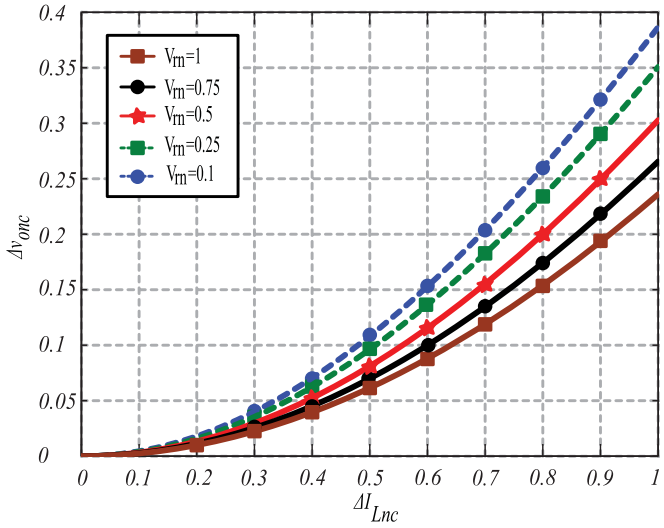

Fig. 11. Normalized output voltage's variation versus the removed load from the converter.

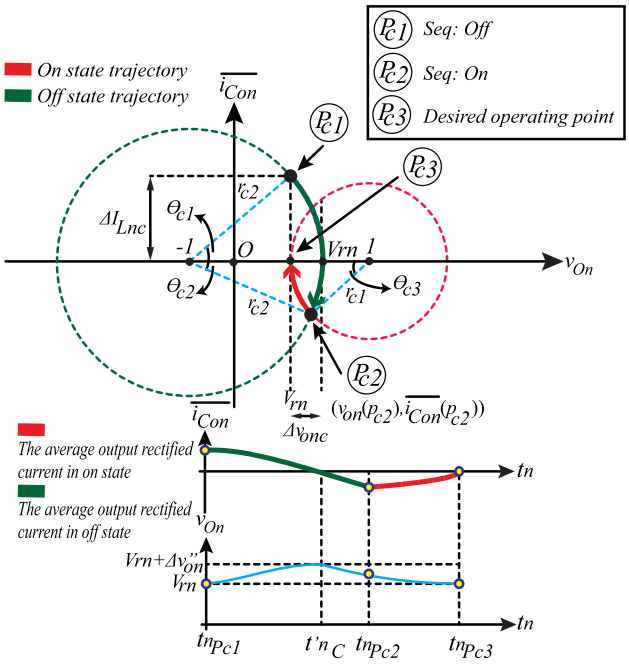

Fig. 10. Converter's transient response to load step-down in state plane and time domain.

shown in Fig. 10. At the intersection of the ON and OFF state trajectories which is the point P_{c2}, S_{eq} turns ON and causes the converter to follow the ON state trajectory. Finally, at the point P_{c3}, the output voltage meets the desired operating point. The angles θ_{c1}, θ_{c2}, and θ_{c3} are given by the following equations:

$$\theta_{c1} = \cos^{-1}\left(\frac{1+V_{rn}}{\sqrt{\Delta I_{Lnc}^2+(1+V_{\text{inn}})^2}}\right) \tag{51}$$

$$\theta_{c2} = \cos^{-1}\left(\frac{1+V_{rn}+(1/4)\Delta I_{Lnc}^2}{\sqrt{\Delta I_{Lnc}^2+(1+V_{\text{inn}})^2}}\right) \tag{52}$$

$$\theta_{c3} = \cos^{-1}\left(\frac{1-V_{rn}-(1/4)\Delta I_{Lnc}^2}{1-V_{rn}}\right). \tag{53}$$

Therefore, the required time for the converter to reach to the desired operating point can be calculated by use of the following equation:

$$t_{nLS-D} = \frac{T_{\text{eq}}}{2\pi}(\theta_{c1}+\theta_{c2}+\theta_{c3}). \tag{54}$$

Also, the output voltage variation after applying load step-down is given by the equation below:

$$\Delta v_{Onc} = -(1+V_{rn}) + \sqrt{\Delta I_{Lnc}^2+(1+V_{rn})^2}. \tag{55}$$

In Fig. 11, the variation of the normalized output voltage versus load variation for different reference voltages is plotted.

The next scenario is the sudden reference and input voltage changes. Because all the voltages are normalized by the input voltage, discussing on the converter's dynamic response to the sudden reference voltage change is valid for the sudden input voltage change. For this reason, Figs. 12 and 13 are utilized. First of all, the converter's dynamic response in abrupt reference voltage decrement (abrupt input voltage increment) is analyzed and after that the dynamic of the converter's model to the sudden reference voltage increment (sudden input voltage decrement) will be discussed. As shown in Fig. 12, after suddenly reducing the reference voltage from V_{rnd0} to V_{rnd1}, S_{eq} turns OFF and causes the converter to follow the OFF state trajectory. At the point P_{d2}, the two trajectories intersect each other. Therefore, at this point, S_{eq} turns ON which provides an opportunity for the converter to follow the ON state trajectory. Eventually, at the point P_{d3}, the converter meets the new desired operating point. The angles θ_{d1} and θ_{d2} are given as follows:

$$\theta_{d1} = \cos^{-1}\left[\frac{1-v_{On}(P_{d2})}{1-V_{rnd1}}\right] \tag{56}$$

$$\theta_{d2} = \cos^{-1}\left[\frac{1+v_{On}(P_{d2})}{1+V_{rnd1}}\right] \tag{57}$$

where

$$v_{\text{on}}(P_{d2}) = \frac{1}{4}\left[(1+V_{rnd0})^2+(1-V_{rnd1})^2\right]. \tag{58}$$

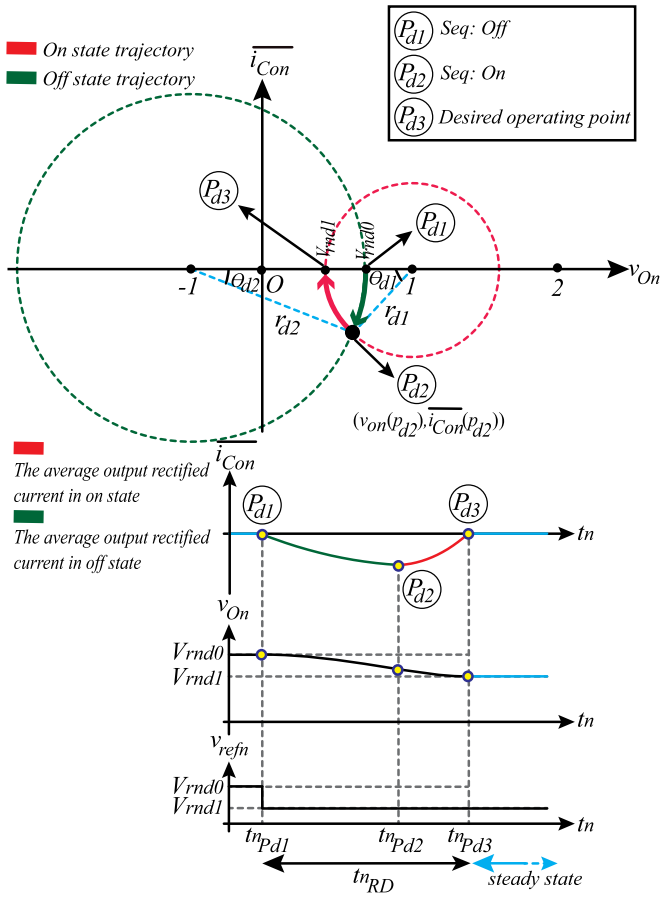

Fig. 12. Converter's transient response to reference voltage decrement (input voltage increment) in state plane and time domain.

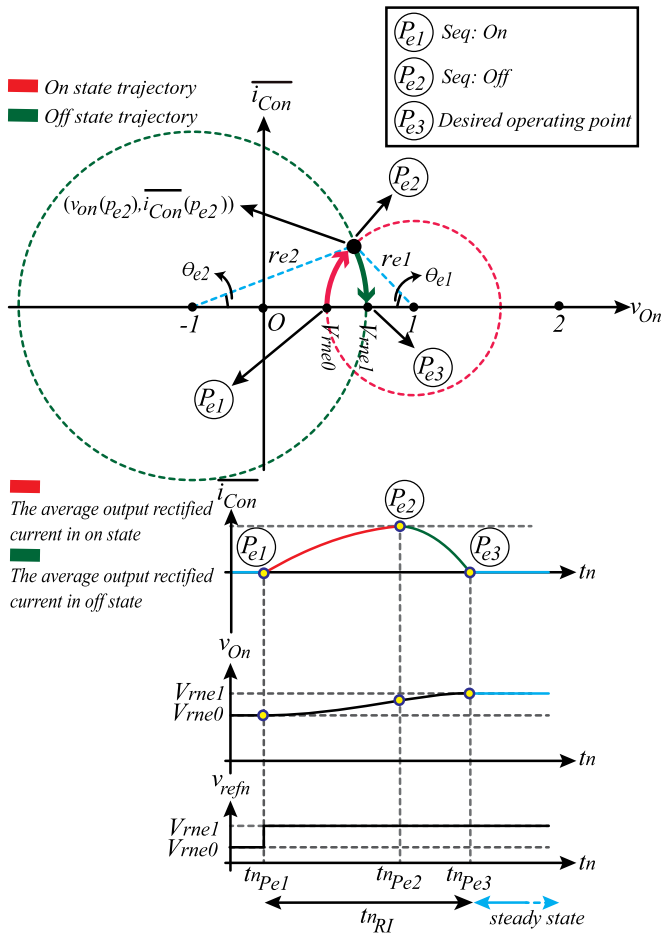

Fig. 13. Converter's transient response to reference voltage increment (input voltage decrement) in state plane and time domain.

By Use of (56) and (57), the interval in which the converter reaches to the desired operating point after applying the sudden reference voltage decrement can be calculated as follows:

$$t_{RD} = \frac{T_{\rm eq}}{2\pi}(\theta_{d1} + \theta_{d2}). \tag{59}$$

In Fig. 13, the dynamic response of the converter's model in the abrupt reference voltage increment is illustrated. After sudden increasing the reference voltage from V_{rne0} to V_{rne1}, $S_{\rm eq}$ turns ON and causes the converter to follow the ON state trajectory as shown in Fig. 13. At the point P_{e2}, the intersection between the ON and OFF state trajectories, $S_{\rm eq}$ turns OFF, which enables the converter to follow the OFF state trajectory. At the point P_{e3}, the converter reaches to the desired operating point. The angles θ_{e1} and θ_{e2} can be calculated by use of the equations below

$$\theta_{e1} = \cos^{-1}\left[\frac{1 - v_{On}(P_{e2})}{1 - V_{rne0}}\right] \tag{60}$$

$$\theta_{e2} = \cos^{-1}\left[\frac{1 + v_{On}(P_{e2})}{1 + V_{rne1}}\right] \tag{61}$$

where

$$v_{On}(P_{e2}) = \frac{1}{4}\left[(1 + V_{rne1})^2 + (1 - V_{rne0})^2\right]. \tag{62}$$

By use of (60) and (61), the interval in which the converter converges to the new desired operating point can be calculated as follows:

$$t_{RI} = \frac{T_{\rm eq}}{2\pi}(\theta_{e1} + \theta_{e2}). \tag{63}$$

All the previous discussions on the converter's average large-signal model enable the AGC law to be obtained. If the boundaries of the ON and OFF state trajectories of the converter's model are shown by $\sigma_{\rm on}$ and $\sigma_{\rm off}$, the proposed controller algorithm according to the current direction in C_O can be easily obtained as shown in Fig. 14. It is interesting to note that the geometric control law is just a simple circle equation that is easy to implement as discussed in the following:

$$\sigma_{\rm on} = \overline{i_{Con}}^2(t_n) + [v_{On}(t_n) - 1]^2 - [1 - V_{rn}]^2 \tag{64}$$

$$\sigma_{\rm off} = \overline{i_{Con}}^2(t_n) + [v_{On}(t_n) + 1]^2 - [1 + V_{rn}]^2. \tag{65}$$

V. AGC Transient Strategy

The implementation of the proposed large-signal average theory and the AGC law are presented in this section. Fig. 15 depicts a conceptual diagram of the control strategy, including the measurement of the output voltage and output current required

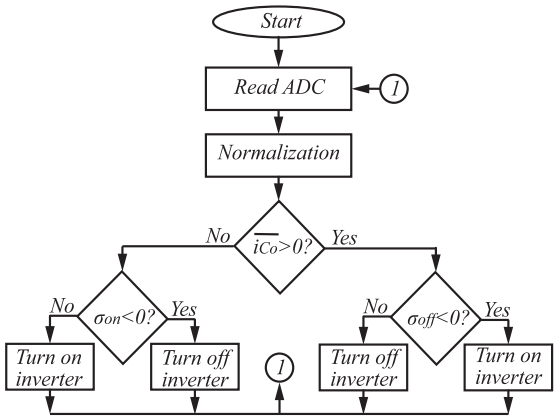

Fig. 14. Control law flowchart.

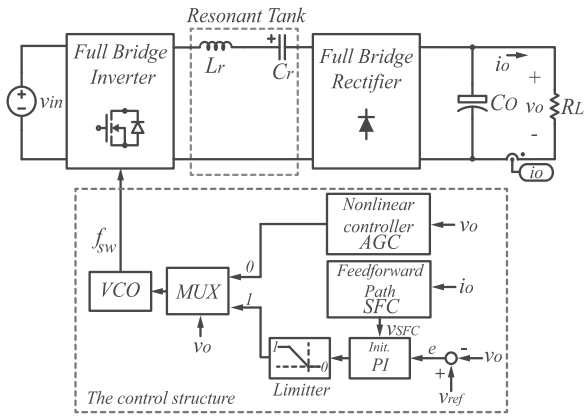

Fig. 15. Conceptual block diagram and sensing strategy for the control structure.

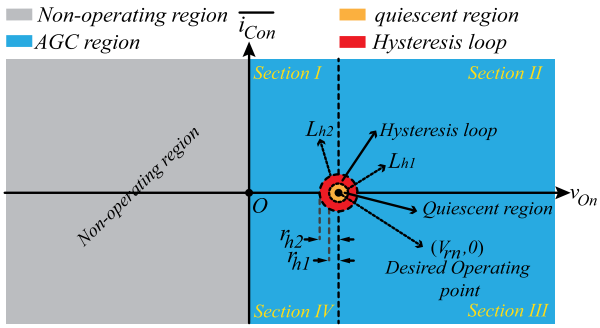

Fig. 16. Different operating regions of the converter in state plane.

to resolve transients with high performance, operate in steady state, and protect the converter (overload). The control structure in Fig. 15 allows the SRC to operate in geometric mode (AGC) and quiescent mode and it is employed for testing, comparison, and validation. Fig. 16 exhibits the different regions on the state plane showing the small-signal quiescent region (orange region) and the large-signal region (blue region). When the converter is within the quiescent region, a simple controller (e.g., PI) can perform properly in steady state. However, when the system operates away from the quiescent region, the transient is resolved with high performance by the AGC law and directs the operating point toward the target. Once the transient is resolved, any simple linear controller can be used to manage the steady and quiescent operation using frequency modulation. The merit of using the frequency modulation after the resonant frequency is the provided ZVS condition for the converter's switches.

As discussed in the theory, the AGC forces the converter to follow a circular trajectory to arrive to the target quiescent area. According to (64) and (65), the average current through the output capacitor i_{Co} participates in the control decisions of the AGC. Since the average i_{Co} can actually be derived by only sensing the output voltage ($i_{Co} = C_O dv_O/dt$), there is no need to use a current sensor for measuring i_{Co}. However, if extra accurate performance is needed, a current sensor can be used to measure the average i_{Co} rather than estimating it. Moreover, in most cases, the input voltage of the converter is almost constant and usually has a very small variation. Therefore, by knowing the value of the input voltage, the input voltage is not necessary to be sensed. However, in applications with the large variation in the input voltage, the input voltage can be sensed and employed as part of the AGC in (64) and (65). Once the transient large-signal dynamics are completed with the AGC, the converter enters the small-signal quiescent region. If a simple linear PI controller is employed for steady-state operation, the transition between AGC to linear can be done with a switching frequency calculator (SFC). The SFC calculates the appropriate switching frequency to initialize the linear controller according to gain of the SRC [31]

$$\omega_n \approx \frac{1}{2Q}\left[\sqrt{\frac{0.9^2}{M_v}-1}+\sqrt{\frac{0.9^2}{M_v}+4Q^2-1}\right] \tag{66}$$

where M_v is V_r/V_{in} or V_{rn}. In order to calculate the appropriate switching frequency in (66), the quality factor Q is required. Therefore, the current through the load should be measured. The advantages of sensing the load current are the provided soft transition between the AGC and quiescent regions and protection against short circuit. Also, to prevent chattering in the boundary of the AGC and linear regions, a hysteresis loop should be employed. As shown in Fig. 16, the quiescent region is determined by the circle L_{h1} with the radius of r_{h1}. The outer circle L_{h2} with the radius of r_{h2} determines the band of the hysteresis loop which can be calculated by $r_{h2} - r_{h1}$.

VI. Design Considerations

In Section II, it was theoretically shown that the full-bridge SRC can be modeled with the converter shown in Fig. 4. To benefit the introduced model for controlling the converter using the proposed AGC method, the output voltage and the load current must be measured. The derivative of the output voltage can be used to measure the current through the output capacitor. Also, because the current through C_O has two frequency components (a higher one and a lower one) and based on the need to extract the frequency component with the lower frequency, a low-pass filter should be used. If the ratio between ω_0 and ω_{eq} is named

ρ ($\omega_0 = \rho\omega_{\rm eq}$), it can be shown that ρ is obtained by

$$\rho = \frac{180}{\cos^{-1}\left(1 - 2\frac{C_{\rm eq}}{C_O}\right)}. \tag{67}$$

Since in practice C_O is much larger than C_r and also $C_{\rm eq}$, ρ is a large value which shows $\omega_0 \gg \omega_{\rm eq}$. Therefore, the difference between the two frequency components is very high which makes the extraction of the low-frequency component easy and also causes the microprocessor to not need a fast computational ability. Accurate signal processing of the capacitor current i_{Co} involves filtering the high resonant frequency properly and obtaining the low-frequency component while maintaining the low-phase shift to make the AGC method effective. Hence, to keep the phase delay close to zero, the cut off frequency of the low-pass filter should be much larger than $\omega_{\rm eq}$. In simple terms $\omega_{\rm eq} \ll \omega_{\rm cut} < \omega_0$, where $\omega_{\rm cut}$ is the cut off angular frequency of the low-pass filter. Conclusively, a second-order filter with the damping factor of 1 and the cut off angular frequency of $(\omega_0 + \omega_{\rm eq})/2$ can be selected with the following transfer function

$$F(s) = \frac{1}{\left(1 + \frac{2s}{\omega_0 + \omega_{\rm eq}}\right)^2}. \tag{68}$$

The phase delay that the selected second-order low-pass filter imposes to the system can be calculated by use of the equation below

$$\Phi = -2\tan^{-1}\left[\frac{2}{1+\rho}\right]. \tag{69}$$

Since ρ is large enough in practice, the produced phase delay is considerably small. Finally, the completed transfer function that can be used to obtain $\overline{i_{Co}}$, is given as follows:

$$H(s) = \frac{\overline{i_{Co}}}{v_o} = sC_O F(s). \tag{70}$$

For the steady-state operation around the quiescent region, a linear PI controller is implemented. The next step is determining the radius of the circles r_{h1} and r_{h2} to create a smooth transition between the fast dynamics AGC and steady operation. Because the PI controller is asymptotically stable and due to the extreme dynamics of the nonlinear controller which are close to the resonant frequency, the radius of the inner circle of the comparator shown in Fig. 16 can be obtained by use of the following equation:

$$r_{h1} > i^{+}_{Copn} - I_{On} \tag{71}$$

where according to Kazimierczuk and Czarkowski [31]

$$i^{+}_{Cop} \approx \frac{2V_{\rm in}}{\pi \underline{R_L}}. \tag{72}$$

In (72), $\underline{R_L}$ is the minimum resistance of the load.

In order to obtain (66), the first harmonic approximation technique is used [31]. Compared to the converter's real voltage gain depicted in Fig. 1(b), (66) shows around 10% error to calculate the switching frequency in steady state. Therefore, the radius of the outer circle of the comparator can be selected $0.1\ V_{rn}$ based on the error of (66).

TABLE I
VALUES OF THE LYAPUNOV FUNCTION'S DERIVATIVE IN DIFFERENT REGIONS OF THE STATE PLANE

Coefficients/Sections	Section I	Section II	Section III	Section IV
$2(v_{On} - V_{rn})u((v_{On} - V_{rn})i_{C\rm on})$	< 0	$= 0$	> 0	$= 0$
$(v_{On} - V_{rn})^2\delta((v_{On} - V_{rn})i_{C\rm on})$	$= 0$	$= 0$	$= 0$	$= 0$
$d(v_{On} - V_{rn})/dt$	> 0	> 0	< 0	< 0
$2i_{C\rm on}[1 - u((v_{On} - V_{rn})i_{C\rm on})]$	$= 0$	> 0	$= 0$	< 0
$(i_{C\rm on})^2\delta((v_{On} - V_{rn})i_{C\rm on})$	$= 0$	$= 0$	$= 0$	$= 0$
$di_{C\rm on}/dt$	$< 0, > 0$	< 0	$> 0, < 0$	> 0
f	< 0	< 0	< 0	< 0

TABLE II
CONVERTER'S PARAMETERS

Converter Parameters	Value
$V_{\rm in}$	48 V
V_O	24 V
f_0	80 kHz
L_r	195 μH
C_r	20 nF

TABLE III
AVERAGE LARGE-SIGNAL MODEL'S PARAMETERS

Converter Parameters	Value
$L_{\rm eq}$	481 μH
C_O	33 μF
$\omega_{\rm eq}$	7.93 Krad/s
$\omega_{\rm cut}$	314 Krad/s
ρ	63.35
Φ	3.65

VII. STABILITY ANALYSIS

The large-signal stability of the AGC controller can be justified using the Lyapunov theorem. According to the control law shown in Fig. 14, the following function ($Y : \Re^2 \to \Re$):

$$\begin{aligned} Y(v_{On} - V_{rn}, i_{C\rm on}) = \ & \left[(v_{On} - V_{rn})^2 u\left((v_{On} - V_{rn})i_{C\rm on}\right)\right. \\ & \left. + i^2_{C\rm on}[1 - u((v_{On} - V_{rn})i_{C\rm on})\right] \end{aligned} \tag{73}$$

can be a Lyapunov-candidate function of the AGC controller with the unique equilibrium point $Y(0,0)$ because

$$Y(0,0) = 0 \tag{74}$$

$$Y(v_{On} - V_{rn}, i_{C\rm on}) > 0 \quad \forall (v_{On} - V_{rn}, i_{C\rm on}) \neq (0,0) \tag{75}$$

$$||(v_{On} - V_{rn}, i_{C\rm on})|| \to \infty \Longrightarrow Y(v_{On} - V_{rn}, i_{C\rm on}) \to \infty \tag{76}$$

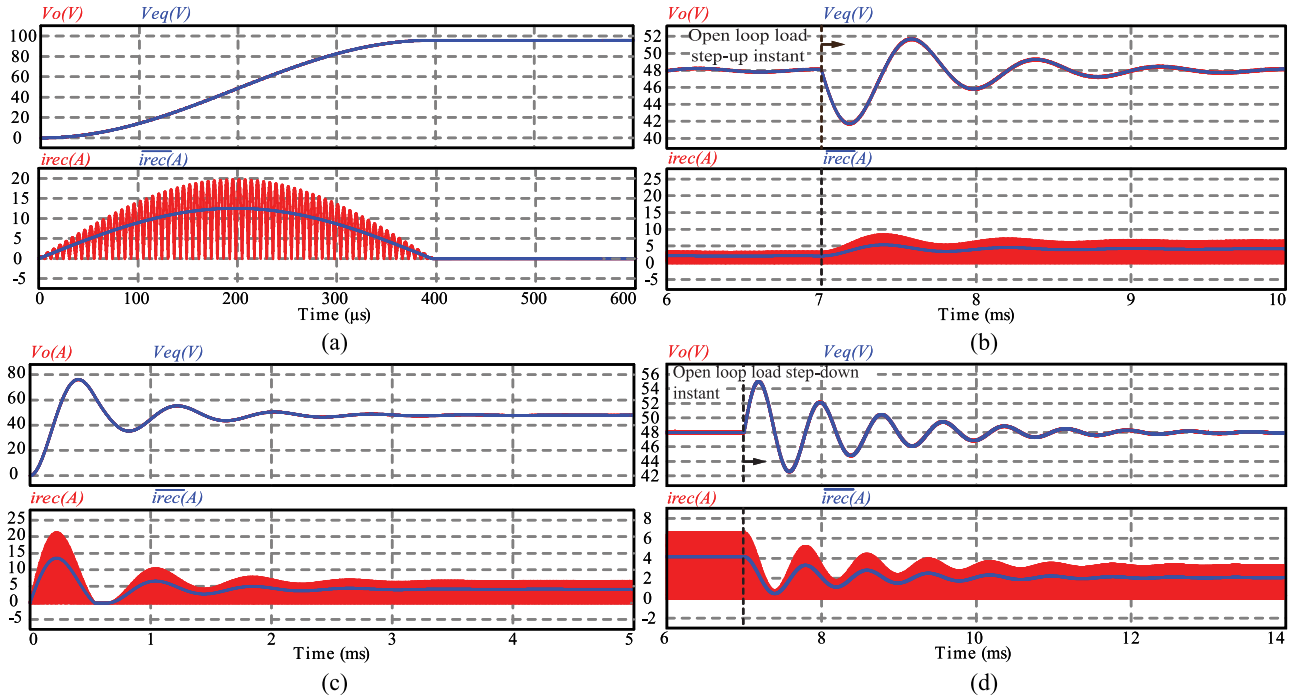

Fig. 17. Open-loop simulation results of the SRC at the resonant frequency and its average large-signal model validating the proposed model. (a) Startup in no-load condition, (b) startup under a 12-Ω load, (c) load step-up from 24 to 12 Ω, (d) load step-down from 12 to 24 Ω.

and

$$\frac{dY(v_{On}-V_{rn},i_{Con})}{dt} = [2(v_{On}-V_{rn})u((v_{On}-V_{rn})i_{Con}) + (v_{On}-V_{rn})^2\delta((v_{On}-V_{rn})i_{Con})] \times \frac{d(v_{On}-V_{rn})}{dt} + [2i_{Con}[1-u((v_{On}-V_{rn})i_{Con})] - (i_{Con})^2\delta((v_{On}-V_{rn})i_{Con})] \times \frac{di_{Con}}{dt} < 0 \quad (77)$$

where

$$u((v_{On}-V_{rn})i_{Con} = \begin{cases} 0, & \text{if } (v_{On}-V_{rn})i_{Con} > 0 \\ 1, & \text{if } (v_{On}-V_{rn})i_{Con} \le 0 \end{cases} \quad (78)$$

and

$$\delta((v_{On}-V_{rn})i_{Con}) = \begin{cases} 0, & \text{if } (v_{On}-V_{rn})i_{Con} \neq 0 \\ \infty, & \text{if } (v_{On}-V_{rn})i_{Con} = 0. \end{cases} \quad (79)$$

The condition (77), referred to as the monotonicity requirement of the Lyapunov theorem, is always satisfied by the control algorithm shown in Fig. 14, and it can be geometrically explained by dividing the state plane shown in Fig. 16 into four sections. In Table I, the values of the coefficients of (77) for different sections are presented. Therefore, $Y(v_{On}-V_{rn},i_{Con})$ is globally asymptotically stable.

To design the linear compensator, there are two strategies that can be used. The first is to use small-signal models obtained for the SRC. Until now, many small-signal models have been introduced for the SRC that are very complicated. The second strategy is to use heuristic methods that are proper for very complicated plants where describing them mathematically is too complex. Therefore, to design the linear PI controller, the Ziegler–Nichols tuning method can be employed, ensuring the stability of the system in the equilibrium area [30].

The final step to ensure the stability of the system is in the selection of the hysteresis band. The instructions on how to appropriately select the boundaries of the hysteresis loop can be found in Section VI.

VIII. Simulation and Experimental Results

A. Average Large-Signal Validation

In Section II, the average large-signal model was introduced and a method was proposed to obtain the value of $L_{\rm eq}$. Because the average large-signal model is intended to be engaged as the core of the proposed AGC controller, the accuracy of the average large-signal model must be justified. Therefore, in order to validate the average large-signal model, the simulation results of the open-loop SRC and its average large-signal model are presented in this section. To simulate the SRC and average large-signal model, PSIM software was used. The parameters of the SRC and its average large-signal model can be found in Tables II and III. Fig. 17 shows the key simulation waveforms of the SRC and average large-signal model in four cases: including start up in no load and under the load conditions, load step-up, and load step-down. The simulation results prove that the average large-signal model precisely follows the open-loop dynamic behavior of the SRC if the switching frequency equals

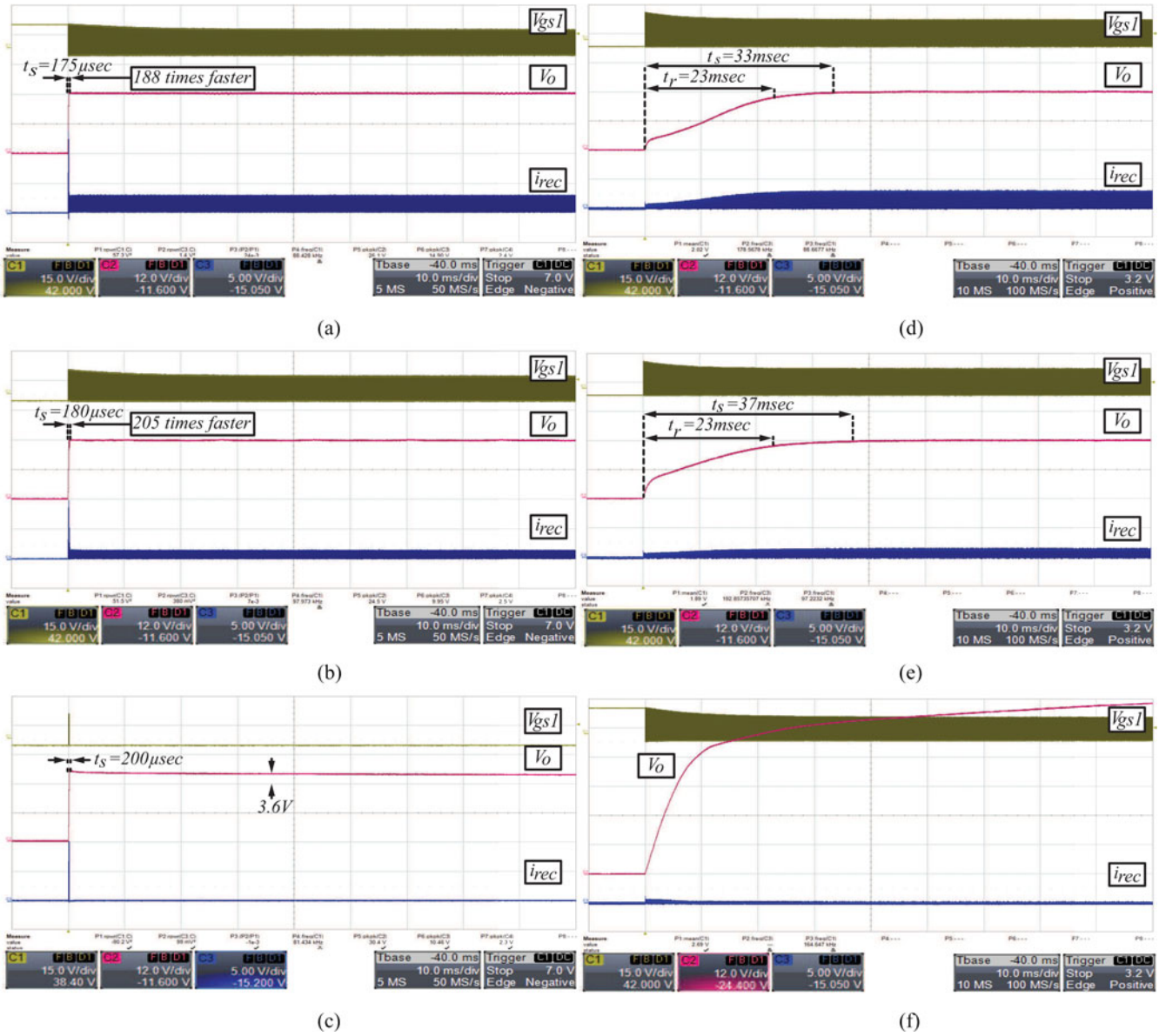

Fig. 18. Comparative experimental validation of the SRC dynamic transient using the proposed AGC versus a linear PI controller: (a) SRC in start up and under 50-W resistive load using the proposed AGC, (b) startup under 25-W resistive load using AGC, (c) startup under no load using AGC. SRC converter response using (d) PI controller in start up and under 50-W resistive load, (e) PI controller in start-up and under 25-W resistive load, and (f) PI controller in start-up and no-load condition.

the resonant frequency. In the waveforms shown in Fig. 17, the output voltages of the SRC and average large-signal model are always equal over the time, and the current through the equivalent inductor follows the average dynamic of the output rectified current.

B. Close-Loop Experimental Results

In order to validate the theoretical analysis, the experimental results of a 50-W prototype full-bridge SRC are presented in this section and the proposed geometric control method is employed. Also, to compare the effectiveness of the proposed control method with a conventional linear controller, the experimental results of an SRC controlled with a PI controller are included. The converter and average large-signal model's parameters are shown in Tables II and III, respectively. The radius of the circles L_{h1} and L_{h2} (r_{h1} and r_{h2}) that are introduced in Section V are selected as 0.03 and 0.05 in the normalized state plane, respectively.

One of the main advantages of the proposed AGC controller is its ability to prevent voltage overshoot following disturbances. Therefore, to compare the performance of the proposed controller with that of a linear controller, this criterion (prevention of voltage overshoot) should be taken into account during the design of the linear controller. To design the linear PI compensator, the Ziegler–Nichols tuning method is used. The transfer function of the PI controller is chosen as follows:

$$C(s) = \frac{1}{24}\left[0.2 + \frac{400}{s}\right]. \tag{80}$$

Moreover, since the proposed AGC controller is a nonlinear controller, it is appropriate to compare the proposed controller with an advanced nonlinear controller. Therefore, the RSS control method [21] (an advanced control method based on a piecewise affine model) is selected. The RSS controller controls the SRC by monitoring the converter's behavior in state plane, where the slope of a line determines the instant when switching actions occur. The RSS controller has two control loops: inner and outer. The outer loop, which is a linear controller, is responsible for providing the slope of the line in state plane. The inner loop is a nonlinear controller that controls the switching actions by using the slope obtained from the outer loop. In order to employ the RSS control method to control the SRC, the current through the resonant inductor, the voltage of the resonant capacitor, and the output voltage must be measured.

At first, the start-up response of the converter will be discussed. In Fig. 18(a)–(c), the start-up response of the SRC employing the proposed geometric controller is presented under a 50-W resistive load [see Fig. 18(a)], a 25-W resistive load [see Fig. 18(b)], and no-load condition [see Fig. 18(c)]. In the case that the converter is loaded with a 50-W resistive load, the output voltage's rise time is 155 μs and the output voltage's settling time is 175 μs. Under the 25-W resistive load, the output voltage's rise time is 162 μs and the output voltage's settling time is 180 μs. For the same transient, the key experimental waveforms of the SRC employing the conventional PI controller are shown in Fig. 18(d)–(f), where the converter is loaded with a 50-W resistive load [see Fig. 18(d)], 25-W resistive load [see Fig. 18(e)], and no-load [see Fig. 18(f)]. In the case that the converter is loaded with the 50-W and 25-W resistive loads, the output voltage's rise time is 23 ms; however, its settling time under the 50-W resistive load is 33 ms and under the 25-W resistive load is 37 ms. Comparing the time responses of the two SRCs exhibits that the proposed geometric controller in startup is around 200 times faster than the conventional PI controller. Also, in no-load condition, the results show that the output voltage of the SRC controlled with the proposed controller has increased 15% over the reference voltage with the transient time of 200 μs. However, the conventional PI controller in start-up and no-load condition does not show a good performance since the output voltage converges to near the twice of the input voltage. In order to show the SRC's start-up dynamic response with more details, where the proposed controller is engaged, the converter's zoomed in waveforms are presented in Fig. 19(a)–(c) where the converter is loaded with a 50-W resistive load, 25-W resistive load, and no load, respectively.

In the next step, the converter's dynamic response to load step-up and step-down is inspected. In Fig. 20(a) and (b), the dynamic response of the SRC employing the proposed geometric controller is shown to the resistive load step-up from 25 to 50 W and resistive load step-down from 50 to 25 W, respectively. The converter's response time to the both load step-up and step-down is 370 μs. After the load step-up, the output voltage's undershoot is 19.8 V and after the load step-down, the output voltage's overshoot is 28.8 V. For the same transients, the SRC's response to the disturbances, where the conventional PI controller is used, is shown in Fig. 20(c) and (d) for the load step-up and step-down, respectively. In this case, the converter's

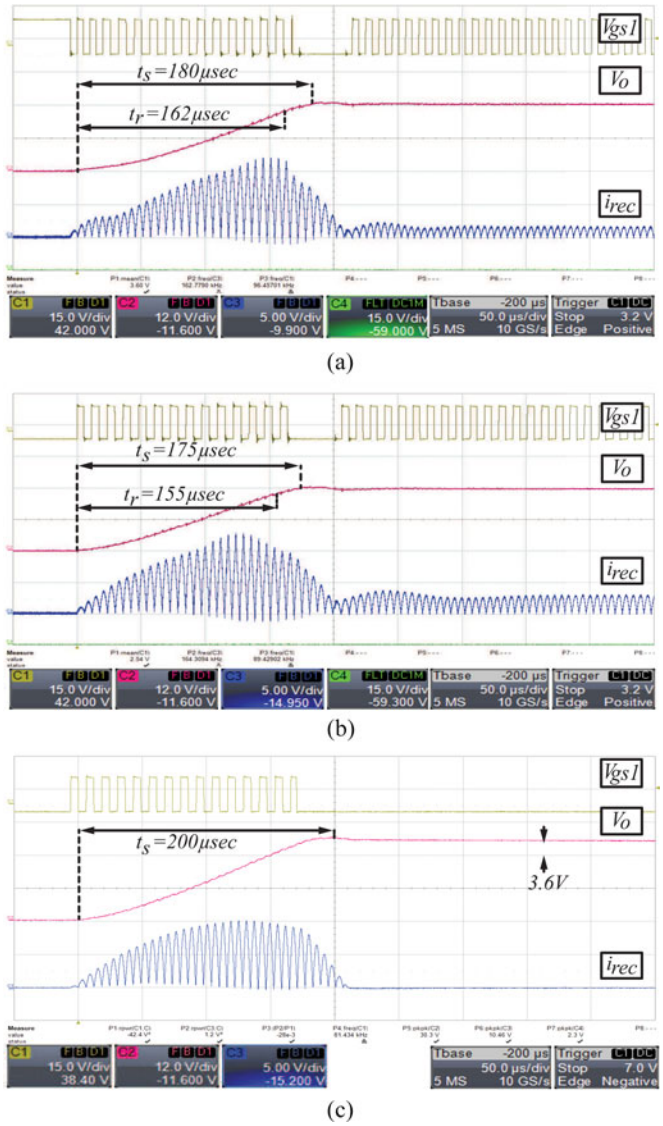

Fig. 19. Zoomed in detailed waveforms of the converter with the proposed controller during start-up under different loading conditions. (a) Under 50-W resistive load, (b) under 25-W resistive load, (c) no-load condition.

response time to the load step-up is 20 ms and to the load step-down is 17.5 ms. The output voltage's undershoot after the load step-up is 16.8 V and the output voltage's overshoot after the load step-down is 30 V. Therefore, the proposed controller is around 50 times faster than the conventional PI controller to responding the disturbances, in addition to the improved output voltage's undershoot after the load step-up by 12.5% and output voltage's overshoot after the load step-down by 5%. In order to show the dynamic response of the SRC employing the proposed geometric controller to the load step-up and step-down with more details, in Fig. 21(a) and (b), the converter's zoomed in waveforms are presented. For the same transients, the dynamic response of the close-loop SRC converter controlled with the RSS controller is shown in Fig. 21(c) and (d). The response time is 1.7 ms and the undershoot is 20 V after the load step-up. The waveforms shown in Fig. 21(a) and (c) reveals that the response time of the proposed AGC controller is 4.6 times faster than that of the RSS controller. In Fig. 21(d), the response

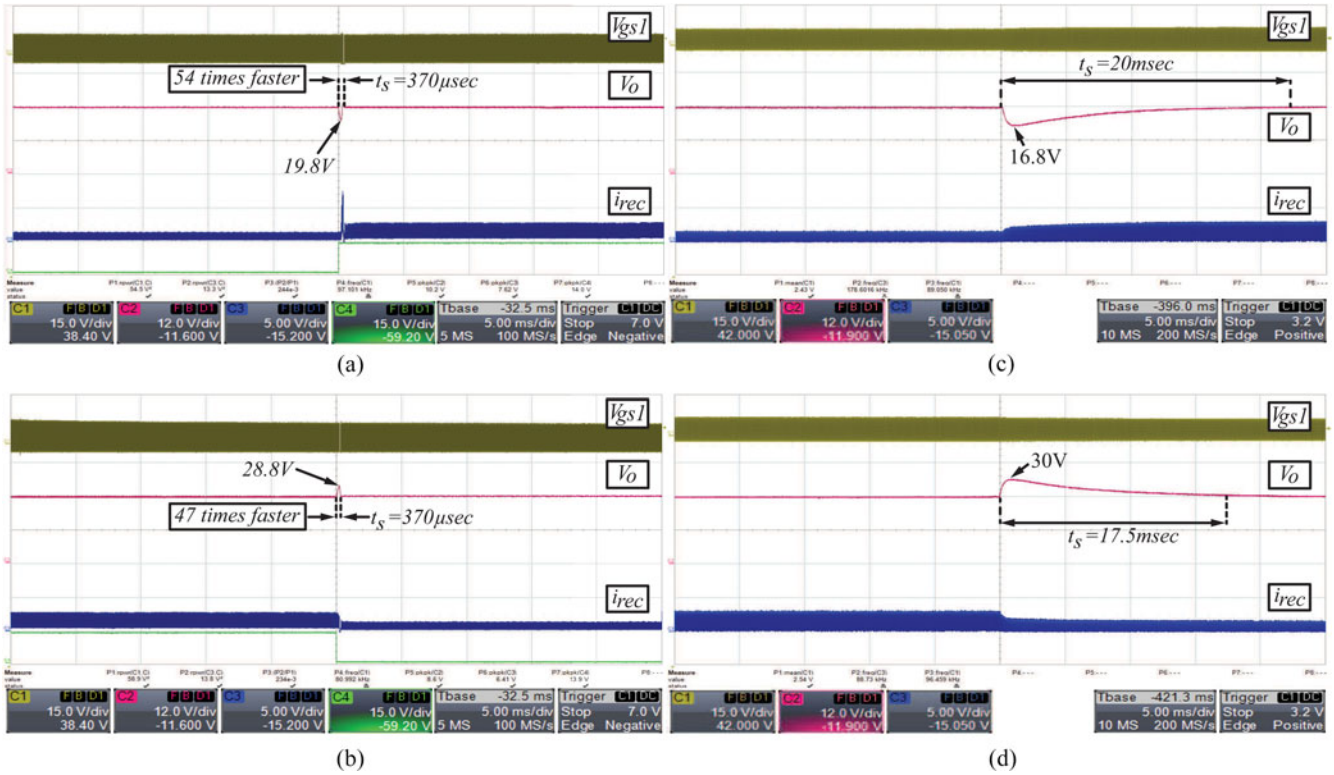

Fig. 20. Load transient comparative experimental validation using the proposed AGC versus a linear PI controller: (a) sudden step-up load change with the proposed AGC, (b) sudden step-down load change with AGC, (c) load step-up with the PI controller, and (d) load step-down with the PI controller.

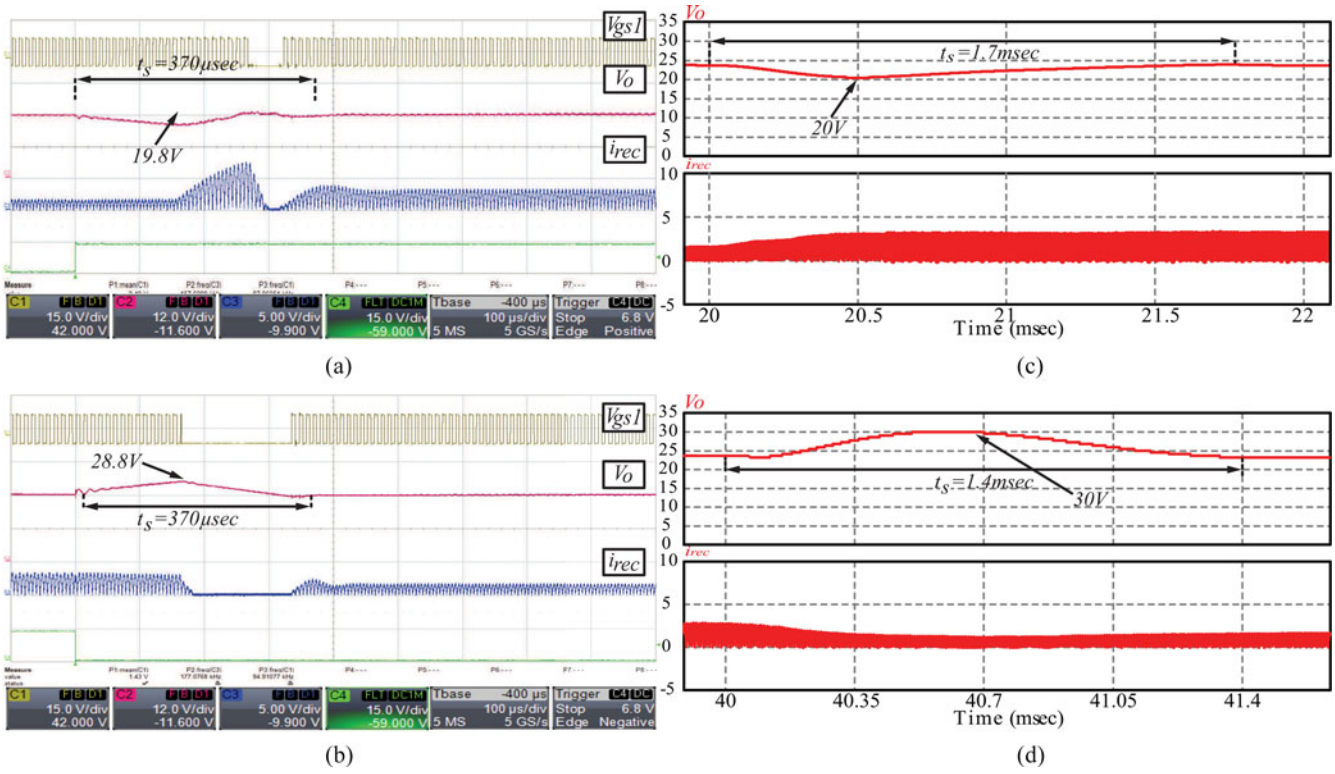

Fig. 21. Zoomed in detailed waveforms of the converter employing the proposed AGC strategy, (a) after the load step-up and (b) after the load step-down. The transient response of the converter employing the RSS controller, (c) after the load step-up and (d) after the load step-down.

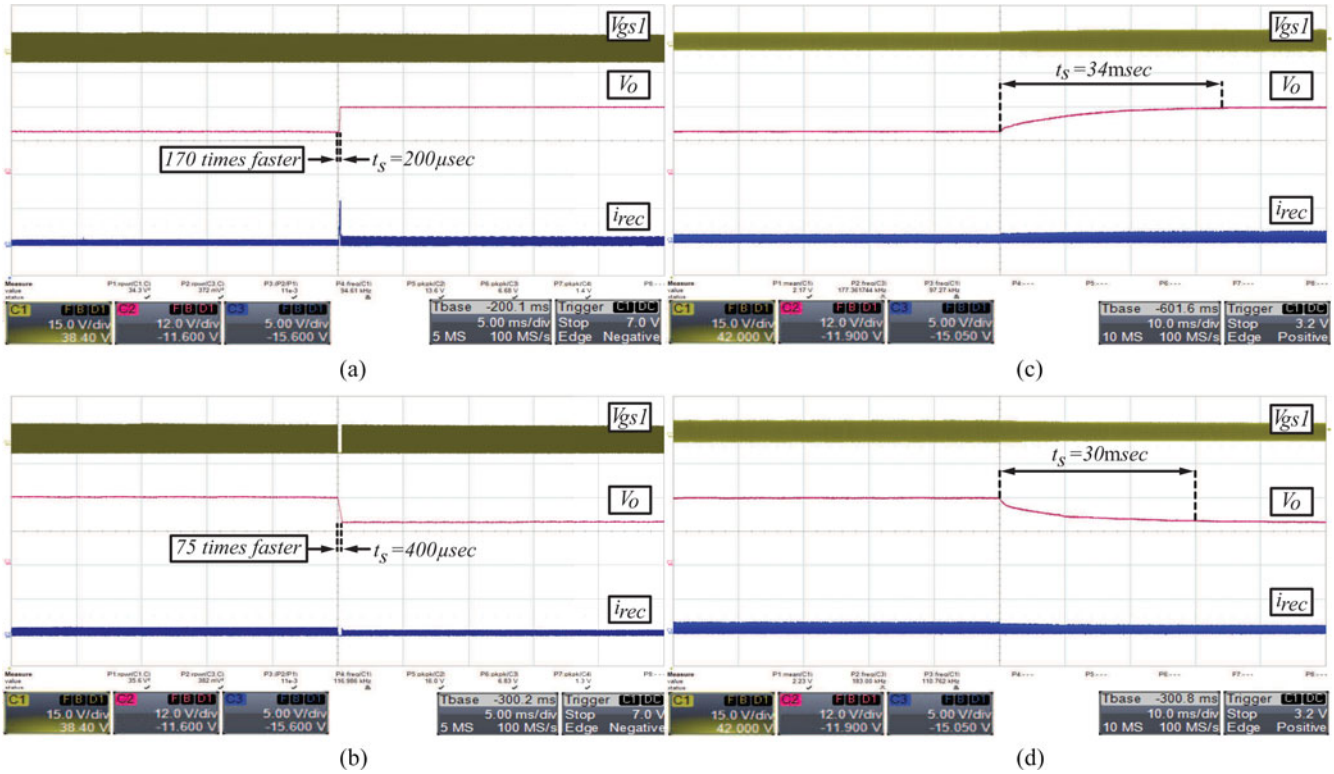

Fig. 22. Reference change comparative experimental validation with the proposed AGC versus a linear PI controller: (a) voltage reference step-up using the proposed AGC, (b) voltage reference step-down using AGC, (c) voltage reference step-up using PI, and (d) voltage reference step-down using AGC.

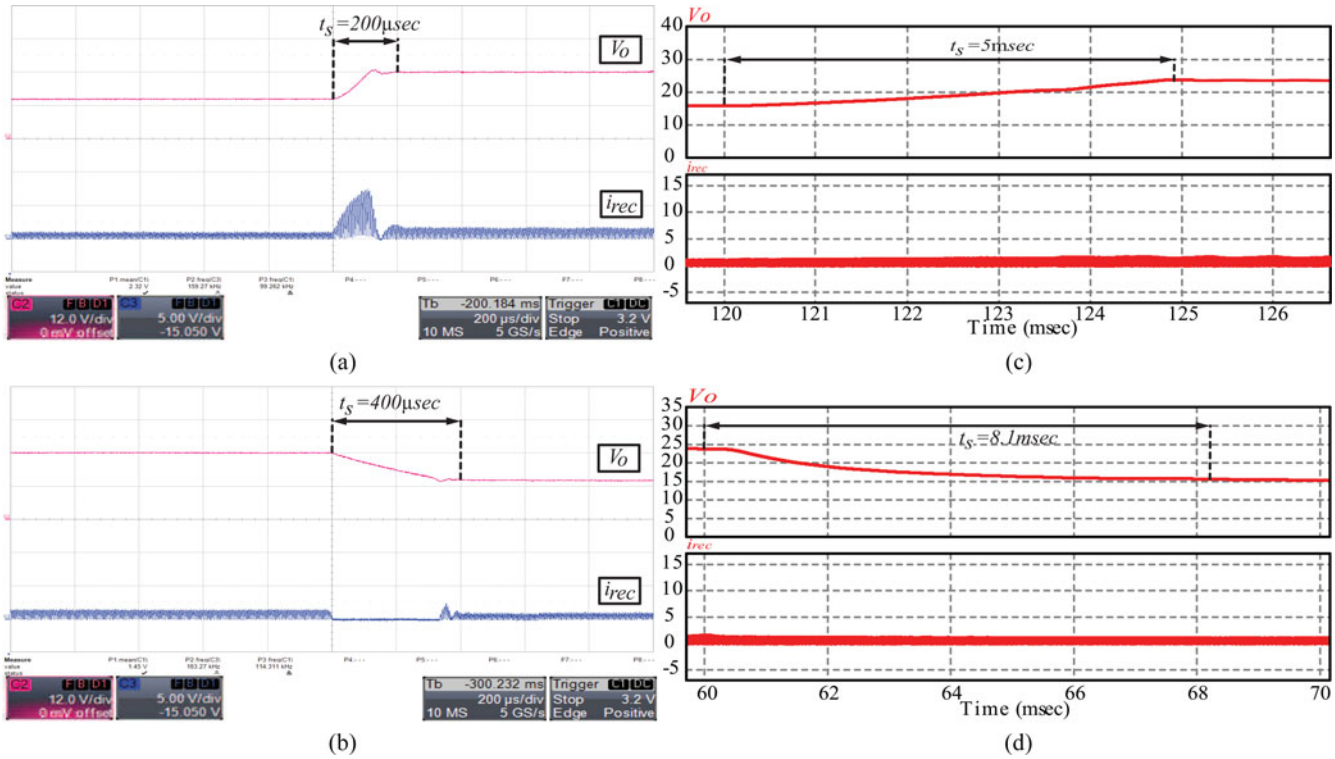

Fig. 23. Zoomed in detailed waveforms of the converter employing the proposed AGC strategy, (a) after the reference voltage step-up and (b) after the reference voltage step-down. The dynamic response of the converter employing the RSS controller, (c) after the reference voltage step-up and (d) after the reference voltage step-down.

of the converter controlled by the RSS controller after a load step-down from 50 to 25 W is shown. The response time of the system after the load step-down is 1.4 ms and the overshoot is 30 V. For the same transient, the response time of the proposed AGC controller is 370 μs and the overshoot is 28.8 V.

In the next experiment, the converter's performance to the sudden referene voltage change was investigated. In Fig. 22(a) and (b), the response of the converter employing the proposed controller to the sudden reference voltage change from 15 to 24 V and from 24 to 15 V is shown where the converter is under a 25-Ω resistive load, respectively. The response time of the system to the reference voltage step-up is 200 μs and to the reference voltage step-down is 400 μs. In Fig. 22(c) and (d), the response of the converter controlled with the PI controller to the same disturbances is shown. As it is indicated in Fig. 22(c) and (d), the response time of the converter to the reference voltage step-up is 34 ms and to the reference voltage step-down is 30 ms. These results show that compared to the conventional PI controller, the proposed controller is 175 times faster at responding to the reference voltage step-up, and 75 times faster at responding to the reference voltage step-down. In order to show the dynamic response of the SRC controlled with the proposed geometric controller with more details, in Fig. 23(a) and (b), the converter's zoomed in waveforms are shown after applying the sudden reference voltage changes. In Fig. 23(c) and (d), the dynamic responses of the converter controlled with the RSS controller are presented after a reference voltage step-up from 15 to 24 V, and after a reference voltage step-down from 24 to 15 V. The response time of the close-loop SRC after the reference voltage step-up is 5 ms, and after the reference voltage step-down is 8.1 ms.

IX. Conclusion

The traditional technique to control the power electronic converters for many years has been based on the linear controllers which use small-signal modeling technique. Since the small-signal models are just valid near the desired operating point, the converter's response to large transients is usually poor; however, it provides a good behavior in steady state. In this paper, a nonlinear control method called AGC was proposed to provide a robust and fast dynamic response for the SRC with the availability of low-cost microprocessors. In order to provide an analytical tool for analyzing the converter's large-signal behavior, an average large-signal model was introduced enabling the average circular trajectories of the SRC to obtain that eventuated in a control law called AGC. On average, the experimental results of the proposed geometric control method showed that the converter's response to disturbances, including load and reference voltage changes and also startup, is over 100 times faster than that of the designed linear PI controller. Moreover, the overshoot after disturbances was virtually eliminated.

References

[1] D. L. OSullivan, M. G. Egan, and M. J. Willers, "A family of single-stage resonant AC/DC converters with PFC," *IEEE Trans. Power Electron.*, vol. 24, no. 2, pp. 398–408, Feb. 2009.

[2] Q. Huang, K. Shi, X. Jia, C. Hu, and D. Xu, "A Bi-directional resonant DC/DC converter with frequency tracking control," in *Proc. IEEE Energy Convers. Congr. Expo.*, Sep. 2014, pp. 4748–4754.

[3] S. Abe, T. Ninomiya, T. Zaitsu, J. Yamamoto, and S. Ueda, "Seamless operation of bi-directional LLC resonant converter for PV System," in *Proc. IEEE Appl. Power Electron. Conf. Expo.*, Mar. 2014, pp. 2011–2016.

[4] R. P. Twiname, D. J. Thrimawithana, U. K. Madawala, and C. Baguley, "A resonant Bi-directional DC-DC converter," in *Proc. IEEE Int. Conf. Ind. Technol.*, Feb. 2014, pp. 307–311.

[5] Y. Tang and A. Khaligh, "Bidirectional resonant DC-DC step-up converters for driving high-voltage actuators in mobile microrobots," *IEEE Trans. Power Electron.*, vol. 31, no. 1, pp. 340–352, Jan. 2016.

[6] X. Wu, C. Hu, J. Zhang, and Z. Qian, "Analysis and design considerations of LLCC resonant multioutput DC/DC LED driver with charge balancing and exchanging of secondary series resonant capacitors," *IEEE Trans. Power Electron.*, vol. 30, no. 2, pp. 780–789, Feb. 2015.

[7] Y. Wang, Y. Guan, K. Ren, W. Wang, and D. Xu, "A single-stage LED driver based on BCM boost circuit and LLC converter for street lighting system," *IEEE Trans. Ind. Electron.*, vol. 62, no. 9, pp. 5446–5457, Sep. 2015.

[8] C.-A. Cheng, H.-L. Cheng, and T.-Y. Chung, "A novel single-stage high-power-factor LED street-lighting driver with coupled inductors," *IEEE Trans. Ind. Appl.*, vol. 50, no. 5, pp. 3037–3045, Sep. 2014.

[9] W. Feng, F. C. Lee, and P. Mattavelli, "Optimal trajectory control of LLC resonant converters for LED PWM dimming," *IEEE Trans. Power Electron.*, vol. 29, no. 2, pp. 979–987, Feb. 2014.

[10] N. Shafiei and M. Ordonez, "Improving the regulation range of EV battery chargers with L3C2 resonant converters," *IEEE Trans. Power Electron.*, vol. 30, no. 6, pp. 3166–3184, Jun. 2015.

[11] J.-Y. Lee, Y.-D. Yoon, and J.-W. Kang, "A single-phase battery charger design for LEV based on DC-SRC with resonant valley-fill circuit," *IEEE Trans. Ind. Electron.*, vol. 62, no. 4, pp. 2195–2205, Apr. 2015.

[12] G. G. Oggier, M. Ordonez, J. M. Galvez, and F. Luchino, "Fast transient boundary control and steady-state operation of the dual active bridge converter using the natural switching surface," *IEEE Trans. Power Electron.*, vol. 29, no. 2, pp. 946–957, Feb. 2014.

[13] I. G. Zurbriggen, M. Ordonez, and M. Anun, "PWM-geometric modelling and centric control of basic DC-DC topologies for sleek and reliable large-signal response," *IEEE Trans. Ind. Electron.*, vol. 62, no. 6, pp. 2297–2308, Apr. 2015.

[14] E. X. Yang, F. C. Lee, and M. M. Jovanovic, "Small-signal modeling of series and parallel resonant converters," in *Proc. 7th Annu. Appl. Power Electron. Conf. Expo.*, Feb. 1992, pp. 785–792.

[15] M. E. Elbuluk, G. C. Verghese, and J. G. Kassakian, "Sampled-data modeling and digital control of resonant converters," *IEEE Trans. Power Electron.*, vol. 3, no. 3, pp. 344–354, Jul. 1988.

[16] C. Q. Lee, K. Siri, and S. J. Fang, "State plane approach to frequency response of resonant convertors," *IEE Proc. Circuits, Devices Syst.*, vol. 138, no. 5, pp. 557–563, Oct. 1991.

[17] Z.-Q. Wang, M. Sznaier, I. Batarseh, and J. Bu, "Robust controller design for a series resonant converter," *IEEE Trans. Aerosp. Electron. Syst.*, vol. 32, no. 1, pp. 221–233, Jan. 1996.

[18] R. Oruganti and F. C. Lee, "Resonant power processors, Part I-State plane analysis," *IEEE Trans. Ind. Appl.*, vol. IA-21, no. 6, pp. 1453–1460, Nov. 1985.

[19] R. Oruganti and F. C. Lee, "Resonant power processors, Part II-Methods of control," *IEEE Trans. Ind. Appl.*, vol. IA-21, no. 6, pp. 1461–1471, Nov. 1985.

[20] R. Oruganti, J. J. Yang, and F. C. Lee, "Implementation of optimal trajectory control of series resonant converter," *IEEE Trans. Power Electron.*, vol. 3, no. 3, pp. 318–327, Jul. 1988.

[21] M. Momeni, H. Meshgin Kelk, and H. Talebi, "Rotating switching Surface control of series-resonant converter based on a piecewise affine model," *IEEE Trans. Power Electron.*, vol. 30, no. 3, pp. 1762–1772, Mar. 2015.

[22] H. Molla-Ahmadian, F. Tahami, A. Karimpour, and N. Pariz, "Hybrid control of DCDC series resonant converters: The direct piecewise affine approach," *IEEE Trans. Power Electron.*, vol. 30, no. 3, pp. 1714–1723, Mar. 2015.

[23] K. K.-S. Leung and H. S.-H. Chung, "A comparative study of boundary control with first- and second-order switching surfaces for buck converters operating in DCM," *IEEE Trans. Power Electron.*, vol. 22, no. 4, pp. 1196–1209, Jul. 2007.

[24] K. K.-S. Leung and H. S.-H. Chung, "Derivation of a second-order switching surface in the boundary control of buck converters," *IEEE Power Electron. Lett.*, vol. 2, no. 2, pp. 63–67, Jun. 2004.

[25] W.-T. Yan, C. N.-M. Ho, H. S.-H. Chung, and K. T. K. Au, "Fixed-frequency boundary control of buck converter with second-order switching surface," *IEEE Trans. Power Electron.*, vol. 24, no. 9, pp. 2193–2201, Sep. 2009.
[26] G. E. Pitel and P. T. Krein, "Minimum-time transient recovery for DC–DC converters using raster control surfaces," *IEEE Trans. Power Electron.*, vol. 24, no. 12, pp. 2692–2703, Sep. 2009.
[27] M. Ordonez, M. T. Iqbal, and J. E. Quaicoe, "Selection of a curved switching surface for buck converters," *IEEE Trans. Power Electron.*, vol. 21, no. 4, pp. 1148–1153, Jul. 2006.
[28] G. Oggier and M. Ordonez, "Boundary control of full-bridge ZVS: Natural switching Surface for transient and steady-state operation," *IEEE Trans. Ind. Electron.*, vol. 61, no. 2, pp. 969–979, Feb. 2014.
[29] M. Anun, M. Ordonez, I. Galiano Zurbriggen, and G. Oggier, "Circular switching surface technique: High performance constant power load stabilization for electric vehicle systems," *IEEE Trans. Power Electron.*, vol. 30, no. 8, pp. 4560–4572, Aug. 2015.
[30] K. Ogata, *Modern Control Engineering*, 5th ed. Englewood Cliffs, NJ, USA: Prentice-Hall, 2010.
[31] M. K. Kazimierczuk and D. Czarkowski, *Resonant Power Converters*, 2nd ed. Hoboken, NJ, USA: Wiley, 2010.

Mehdi Mohammadi (S'14) was born in Isfahan, Iran, in 1989. He received the B.Sc. degree in electronics technology engineering from the Bonyan Institute of Higher Education, Shahinshahr, Iran, in 2010, and the M.Sc. degree in electrical engineering (electronics) from the Isfahan University of Technology (IUT), Isfahan, Iran, in 2014. He is currently working toward the Ph.D. degree at the University of British Columbia (UBC), Vancouver, BC, Canada.

His current research interests include developing infrastructures required for the renewable energies particularly advanced nonlinear control methods and soft switching Technologies.

Mr. Mohammadi received the Best Master of Science Thesis Award in electrical engineering in Iran, awarded by the IEEE Iran section, the Superior Master of Science Thesis Award of the IUT, and the Four Year Fellowship and Graduate Support Initiative Scholarship from UBC, all in 2015.

Martin Ordonez (S'02–M'09) was born in Neuquen, Argentina. He received the Ing. degree in electronics engineering from the National Technological University, Cordoba, Argentina, in 2003, and the M.Eng. and Ph.D. degrees in electrical engineering from the Memorial University of Newfoundland (MUN), St. Johns, NL, Canada, in 2006 and 2009, respectively.

He is currently an Assistant Professor at the Department of Electrical and Computer Engineering, University of British Columbia, Vancouver, BC, Canada. He is also a Canada Research Chair in Power Converters for Renewable Energy Systems, as well as an Adjunct Professor with Simon Fraser University, Burnaby, BC, Canada, and MUN. His industrial experience in power conversion includes research and development at Xantrex Technology, Inc./Elgar Electronics Corporation (now AMETEK Programmable Power), San Diego, CA, USA, Deep-Ing. Electronica de Potencia, Rosario, Argentina, and TRV Dispositivos, Cordoba, Argentina. With the support of industrial funds and the Natural Sciences and Engineering Research Council, he has contributed to more than 60 publications and R&D reports.

Dr. Ordonez is an Associate Editor of the IEEE TRANSACTIONS ON POWER ELECTRONICS, serves on several IEEE committees, and reviews widely for IEEE/IET journals and international conferences. He received the David Dunsiger Award for Excellence in the Faculty of Engineering and Applied Science in 2009 and the Chancellors Graduate Award/Birks Graduate Medal in 2006, and became a Fellow of the School of Graduate Studies, MUN.